

MASTER'S THESIS

Eliashberg Theory for Quantum Critical Points in Metals

David Jonas Moser



Faculty of Physics

Ludwig-Maximilians-Universität München

Supervised by

Prof. Dr. Matthias Punk

March 2020

MASTERARBEIT

Eliashberg-Theorie für quantenkritische Punkte in Metallen

David Jonas Moser



Fakultät für Physik

Ludwig-Maximilians-Universität München

Betreut von

Prof. Dr. Matthias Punk

März 2020

Abstract

In this Master's thesis we study two-dimensional metals in the vicinity of charge density wave order with incommensurate ordering wave vectors $\mathbf{Q} = 2k_{\text{F}}$ that connect two points on the Fermi surface with parallel tangents. We investigate this theory of fermions coupled to a real order parameter using both an analytical and numerical Eliashberg approach. With the help of this finite temperature method, we derive analytic expressions for the fermionic and bosonic self-energies in certain limits. While the former reveals clear non-Fermi liquid behavior, the latter suggests dynamical Fermi surface nesting around the hot spots of our theory. Numerically, we confirm this strange metal behavior and discover strongly increased scattering rates in unexpected regions in momentum space. These ridge-like shapes can be identified as $3k_{\text{F}}$ lines by a further analytical calculation. Moreover, we will once more compare the analytical and the numerical calculations by computing the critical exponent relating the renormalized mass to the temperature with both methods and we report even quantitative agreement.

Acknowledgements

First and foremost I would like to thank my supervisor Prof. Dr. Matthias Punk for proposing this very exciting Master's project to me and his great support throughout the year! I highly appreciate his excellent advice whenever questions came up or problems appeared. I learned a lot in these discussions and am also grateful for the Eliashberg code provided.

Next I would like to express gratitude to my charge density wave companions Dr. Dimitri Pimenov and Johannes Halbinger for their interest in my Master's thesis. I am thankful for their critical thinking and appreciate the time they took to answer questions.

Lastly let me also thank all other members of the Chair of Theoretical Solid State Physics for stimulating discussions, relaxing lunch and coffee breaks as well as providing a pleasant work atmosphere.

Contents

1. Introduction	1
2. Formalism & Methods	3
2.1. Quantum Critical Points	3
2.2. Model	5
2.3. Motivation for Eliashberg Theory	7
2.4. Eliashberg Theory	9
2.5. Iterative Solution	11
3. Biconvex Geometries	13
3.1. Scattering Rate	13
3.2. Renormalized Mass	15
3.3. Sommerfeld Expansion	18
3.4. Imaginary Part of Polarization	19
4. Tight Binding Model	23
4.1. Numerical Setup	23
4.2. Results	25
5. Concavo-Convex Geometries	31
5.1. Scattering Rate	31
5.2. Renormalized Mass	31
5.3. Imaginary Part of Polarization	33
5.4. Scattering Rate Revisited	35
6. Fermi Sheet Model	39
6.1. Numerical Setup	39
6.2. First Results	40
6.3. Dynamical Properties	46
6.4. Renormalized Mass	47
7. Summary & Outlook	51
Appendices	53
References	61

1. Introduction

Phase transitions are frequently encountered in everyday life, for example when boiling water or observing melting snow. These kinds of phase transitions occur as a consequence of temperature variation across a critical temperature, meaning these transitions are entropy-driven phenomena [1, 2]. Typically, we can describe these transitions by an effective theory only based on a few ingredients like analyticity, locality and symmetry. This is of course nothing else than the celebrated Ginzburg-Landau theory – a universal theory for the order parameter alone [2, 3].

During the last few decades, the study of so called quantum phase transitions has become an established research field in condensed matter physics [1, 2, 4] as well as high energy physics [5–7]. In contrast to the above mentioned classical phase transitions, quantum phase transitions no longer occur at finite temperatures, but take place at zero temperature. Therefore they are driven by Heisenberg’s uncertainty principle [1] and have to be controlled by non-thermal parameters like the magnetic field, the pressure or the chemical composition of a material [1, 8].

A particular challenging but very interesting subclass are quantum critical points in metals with reduced dimensionality. For example in two dimensions we know that the so called Hertz-Millis approach breaks down and no effective theory for the order parameter alone exists. As a result, we have to treat fermionic and bosonic degrees of freedom on the same footing [2, 9, 10]. Moreover, it turns out that also other standard treatments like the large N expansion fail for some of these theories [11, 12]. It is exactly this combination of rich (non-Fermi liquid) physics and failure of some standard approaches that drives the search of suitable treatments.

In this Master’s thesis, we study two-dimensional metals in the vicinity of charge density wave (CDW) order with incommensurate ordering wave vectors $\mathbf{Q} = 2k_F$ that connect two points on the Fermi surface with parallel tangents [13–16]. We will investigate this theory of fermions coupled to a real order parameter using both an analytical and numerical Eliashberg approach [17–21] as a promising alternative to random phase approximation treatments [13–15] or renormalization group studies [15, 16]. These systems are not only of theoretical interest but also of experimental relevance, since incommensurate charge density wave order appears for example in some rare-earth tellurides [22, 23] or transition-metal dichalcogenides [24–26].

The remaining part of this Master's thesis is structured as follows. The formal treatment of quantum critical metals in the vicinity to charge density wave order will be introduced in Chapter 2. Apart from stating the model, this section also motivates and introduces Eliashberg theory which is our method of choice to treat the introduced theories both analytically and numerically. In Chapter 3, we will start off the actual investigations by analytically analyzing a hot spot model arising for example from a tight binding dispersion relation. In the following Chapter 4 we will continue the analysis but now from a numerical point of view. Since the numerics behaved differently than one might have expected, we will change the dispersion relation and continue our work with a sheet-like Fermi surface. Again, we will start with an analytical analysis in Chapter 5 and numerically justify our results in the following Chapter 6. The final Chapter 7 provides a summary of the studies done and an outlook to further investigations possible.

2. Formalism & Methods

2.1. Quantum Critical Points

The systems we want to consider in this thesis possess a phase diagram as schematically shown in Fig. 2.1. Let us first focus on the temperature $T = 0$ where only two phases – a disordered, Fermi liquid phase and an ordered, charge density wave phase – exist which are separated by a so called quantum critical point. Transitions between the mentioned phases are made possible by tuning a non-thermal parameter m that is measuring the distance from the quantum critical point at $m = m_c$. As mentioned above, examples of such external parameters are the magnetic field, the pressure or the chemical composition of a material [1, 8]. Since at $T = 0$ solely quantum fluctuations are present, this phase transition is referred to as quantum phase transition.

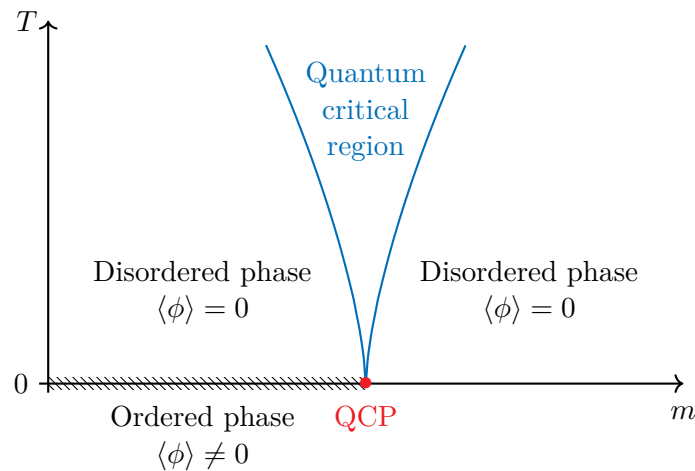


Figure 2.1.: Phase diagram schematically showing the different phases that exist near a quantum critical point (QCP) in strictly two dimensions (in the absence of a Kosterlitz-Thouless transition). The quantum critical point is visualized as a red point and located at temperature $T = 0$ and “mass” $m = m_c$ with m being a non-thermal parameter measuring the distance from the quantum critical point. Figure inspired by [8, 27].

It turns out that quantum critical points are also of great interest for temperatures $T > 0$, since they tend to organize the phase diagram into different regimes or phases.

Therefore, they are not only relevant for zero temperature computations but also for finite temperature calculations or experimental investigations. In Fig. 2.1 this feature can be directly observed, since the two crossover boundaries emerge out of the quantum critical point at $(0, m_c)$. These crossovers can be estimated by comparing the thermal energy $k_B T$ to the typical energy $\hbar\omega_c$ carried by the order parameter field, hence $k_B T \approx \hbar\omega_c$, leading to the following form of the crossover boundaries $T \sim |m - m_c|^{\nu z}$ with ν and z being critical exponents [1, 8, 27]. They enclose the so called quantum critical region or scaling fan being a region where both quantum and thermal fluctuations play an important role. Also note that the quantum critical region's upper boundary can be estimated by $\xi \approx a$ with ξ being the correlation length and a the lattice constant.

The scaling fan will be the region of interest in this thesis, since it hosts rich but also fairly involved non-Fermi liquid physics. The complexity of the problem arises mainly due to the absence of a Ginzburg-Landau-type theory which is of course nothing else than the aforementioned breakdown of the Hertz-Millis theory [1, 2, 9, 10]. This absence of an effective order parameter theory greatly distinguishes metallic QCPs from ordinary QCPs. We will come back to the Hertz-Millis approach in more depth in Section 2.3 and will see that gapless fermions coupled to an order parameter field lie at the heart of this problem.

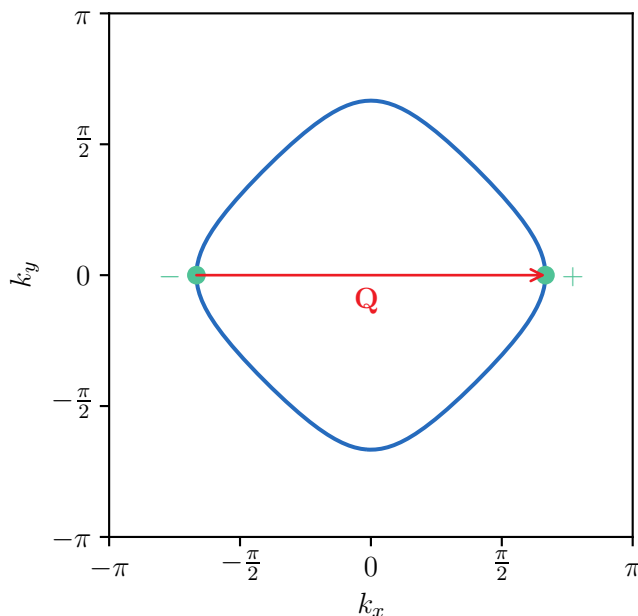


Figure 2.2.: We depict a schematic Fermi surface in blue and a CDW ordering wave vector $\mathbf{Q} = 2k_F$ in red. Furthermore, we show the corresponding hot spots in green. In the following, the right (left) one is typically referred to as the “+” hot spot (“-” hot spot). Figure inspired by [16, 28].

Let us wrap up the discussion of the phase diagram with some comments on charge

density wave order. As Peierls pointed out, this translational symmetry broken phase can already occur in a one-dimensional monoatomic chain at half-filling or equivalently for a Fermi wave vector $k_F = \frac{\pi}{2a}$ [29]. Peierls argumentation goes as follows: Take the standard, equally-spaced monoatomic chain, displace every other atom and calculate the electronic spectrum of the distorted system. It turns out that the spectrum displays a gap at $\pm k_F$ which lowers the groundstate energy of the distorted system compared to the undistorted one. It can be shown that this groundstate energy difference is larger than the energy needed for all the displacements [28, 29]. Therefore, we conclude that the monoatomic chain at half-filling possesses an instability to charge density wave order. This is the so called Peierls instability which leads to a periodic charge density modulation $\langle \bar{\psi}(x)\psi(x) \rangle = n_0 + n_1 \cos(Qx)$ with an ordering wave vector $Q = 2k_F$ [27–29].

Let us come back to two dimensional metals again. Also here, charge density wave order is characterized by a periodically modulated charge density $\langle \bar{\psi}(x)\psi(x) \rangle = n_0 + n_1 \cos(\mathbf{Q} \cdot \mathbf{x})$ with an ordering wave vector $\mathbf{Q} \neq \mathbf{0}$. This is for example in contrast to Ising-nematic ordering where only rotational symmetry is reduced but translational symmetry still unbroken, hence such phases possess ordering wave vectors $\mathbf{Q} = \mathbf{0}$ [2]. Back to finite wave vectors again, we can further categorize them by their “relation” to the Brillouin zone. A commensurate ordering wave vector can be written in the basis of reciprocal lattice vectors with purely rational coefficients [13]. If such a linear combination does not exist, one speaks of incommensurate ordering wave vectors which we will look at in this thesis. Note that this definition also makes sense from a physical point of view, since it has been pointed out that it is important to distinguish between these two types of ordering wave vectors [30, 31]. Lastly, we want to mention that a special situation arises in the presence of so called nesting vectors which are ordering wave vectors connecting two points on the Fermi surface with parallel tangents [13–16]. For this reason, they are also referred to as $2k_F$ wave vectors in the following. A schematic drawing of such a nesting vector and its relation to the Fermi surface is shown in Fig. 2.2.

2.2. Model

The formal starting point of this thesis is provided by the $2 + 1$ dimensional Euclidean action [2, 16]

$$\mathcal{S} = \sum_k \bar{\psi}_k (-i\omega_n + \xi_{\mathbf{k}}) \psi_k + \sum_q \phi_{-q} \chi_q^{-1} \phi_q + \frac{\lambda}{\sqrt{\beta V}} \sum_{k,q} \phi_q \bar{\psi}_{k+q} \psi_k \quad (2.1)$$

where we use the abbreviations $k := (\mathbf{k}, \omega_n)$ and $q := (\mathbf{q}, \Omega_n)$ as well as suppress the spin index for clarity. The reduced dispersion relation is denoted by $\xi_{\mathbf{k}} = \varepsilon_{\mathbf{k}} - \mu$ measuring

the dispersion relation $\varepsilon_{\mathbf{k}}$ relative to the chemical potential μ . Furthermore, ψ is a Grassmann field, ϕ a real order parameter field and $\chi_{\mathbf{q}}$ the corresponding bare boson propagator which may also be referred to as susceptibility. Moreover, λ denotes the coupling constant, $\beta = 1/T$ the inverse temperature and $V = 4\pi^2$ the Brillouin zone's volume. The presented theory of electrons being coupled to a real order parameter via a Yukawa-like interaction can be viewed as emerging from a purely fermionic theory by a Hubbard–Stratonovich transformation in the density channel. Hence, we have traded the four-fermion interaction for a bosonic bilinear together with a Yukawa-like interaction term.

The foregoing model will lay the foundation of all numerical calculation done in this thesis. However, for analytical computations it is easier to work with a low-energy effective theory derived from the action above. In general, one could perform a gradient expansion straight away but would have to take each point on the Fermi surface into account [2]. Assuming a susceptibility χ peaked at momenta $\mathbf{q} = \pm\mathbf{Q}$ – where $\mathbf{Q} = 2k_{\text{F}}$ is an incommensurate nesting vector – leaves us with only two points on the Fermi surface – the so called hot spots – we have to expand around [16]. We therefore introduce the new fields

$$\psi_{\pm, \mathbf{k}, \omega_n} := \psi_{\mathbf{k} \pm \frac{\mathbf{Q}}{2}, \omega_n} \quad (2.2)$$

$$\phi_{\pm, \mathbf{q}, \Omega_n} := \phi_{\mathbf{q} \pm \mathbf{Q}, \Omega_n} \quad (2.3)$$

and expand the dispersion relation

$$\xi_{\mathbf{k} \pm \frac{\mathbf{Q}}{2}} \approx \pm v_{\text{F}} k_x + \frac{\kappa}{2} k_y^2 =: \xi_{\pm, \mathbf{k}} \quad (2.4)$$

where $v_{\text{F}}, \kappa > 0$ denote the Fermi velocity and a constant proportional to the Fermi surface curvature respectively. The resulting biconvex Fermi patch geometry is depicted in Fig. 2.3. Note that the above expansion may for example arise from a tight binding dispersion relation (with appropriate filling).

The last ingredient missing is an explicit expression of the susceptibility which can be approximated by the Ornstein-Zernike form [32]

$$\chi_{\mathbf{q} \pm \mathbf{Q}, \Omega_n}^{-1} \approx m + A\mathbf{q}^2 + B\Omega_n^2 =: \tilde{\chi}_{\mathbf{q}, \Omega_n}^{-1} \quad (2.5)$$

where $A, B > 0$ are temperature-independent prefactors fixing for example the units. m denotes the renormalized mass and fulfills $m \xrightarrow{T \rightarrow 0} 0$, since we approach the quantum critical point right from above. The momentum and frequency dependent terms can be viewed as a low-energy expansion of the polarization's real part. All these approxima-



Figure 2.3.: Visualization of the Fermi surface geometry present in the hot spot model arising e.g. from a tight binding dispersion relation. The black lines depict the Fermi surface patches and each coordinate system's origin is placed right at the hot spot. The red vector \mathbf{Q} connecting these two hot spots illustrates the nesting vector. Moreover, the blue shadings visualize the occupied states at zero temperature.

tions finally give rise to the desired hot spot action [2, 16]

$$\begin{aligned} \mathcal{S}_{\text{HS}} = & \sum_{s=\pm} \sum_k \bar{\psi}_{s,k} (-i\omega_n + \xi_{s,k}) \psi_{s,k} + \sum_q \phi_{-,q} \tilde{\chi}_q^{-1} \phi_{+,q} \\ & + \frac{\lambda}{\sqrt{\beta V}} \sum_{k,q} \left(\phi_{+,q} \bar{\psi}_{+,k+q} \psi_{-,k} + \phi_{-,q} \bar{\psi}_{-,k-q} \psi_{+,k} \right). \end{aligned} \quad (2.6)$$

Note, that we substituted the bosonic fields $\phi_{\pm} \rightarrow \sqrt{2} \cdot \phi_{\pm}$ and rescaled the coupling constant $\lambda \rightarrow \lambda/\sqrt{2}$ for simplicity.

Apart from the tight binding dispersion relation also a second model has been investigated in this Master's project namely a Fermi sheet like dispersion relation. In this case the hot spot model is still valid only the low-energy form of the dispersion relation changes, since now

$$\xi_{\mathbf{k}_{\pm} \frac{\mathbf{Q}}{2}} \approx \pm v_{\text{F},\pm} k_x \mp \frac{\kappa_{\pm}}{2} k_y^2. \quad (2.7)$$

Here $v_{\text{F},\pm}, \kappa_{\pm} > 0$ denote the hot spot dependent Fermi velocities and curvatures. The resulting concavo-convex Fermi patch geometry is depicted in Fig. 2.4.

2.3. Motivation for Eliashberg Theory

The purpose of this section is to give an overview of typical methods used to analyze the models described above and to pave the way for the so called Eliashberg theory introduced in the following section.

As already mentioned above, at first glance it seems quite natural to integrate out the fermionic degrees of freedom (hopefully) resulting in a Ginzburg-Landau-type theory, an effective theory for the order parameter alone. In our context, this was first done



Figure 2.4.: Visualization of the Fermi surface geometry present in the hot spot model arising e.g. from Fermi sheets. The black lines depict the Fermi surface patches and each coordinate system's origin is placed right at the hot spot. The red vector \mathbf{Q} connecting these two hot spots illustrates the nesting vector. Moreover, the blue shadings visualize the occupied states at zero temperature.

by Hertz [9] and later re-examined by Millis [10], hence the name Hertz-Millis theory. Hertz solely looked at the scaling dimension of the quartic order parameter coupling, which turned out to be irrelevant in spatial dimensions $d > 1$ and he concluded that it is safe to integrate out the fermions here [2]. It turned out that this conclusion is wrong in dimensions $d = 2$ and at least hasty in $d \geq 3$, since one also has to take the Yukawa-type coupling of gapless fermions to the order parameter into account. Performing the scaling analysis, one finds for $d \geq 3$ an irrelevant Yukawa coupling and (at least marginally) well-defined quasi-particles (since the fermionic self-energy $\text{Im} \Sigma(\omega) \sim \omega^{d/3}$) such that Hertz-Millis theory remains valid [2]. However in $d = 2$, we encounter a marginal Yukawa coupling and no longer well-defined quasi-particles (since here $\text{Im} \Sigma(\omega) \sim \omega^{2/3}$) such that the Hertz-Millis approach breaks down [2]. Therefore, we are not allowed to integrate out the fermionic degrees of freedom and instead have to apply methods that treat the fermions and the bosons on equal footing [1, 2].

Another standard method is of course a random phase approximation (RPA) which has been investigated for example by Sýkora, Holder and Metzner [13, 14] for the hot spot theory (2.6) stated in the last section. Also their explicit calculations show $\text{Im} \Sigma(\omega) \sim \omega^{2/3}$ and therefore confirm the scaling argument above. Besides plenty of results at leading order they could not manage to obtain self-consistency going beyond leading order. Especially this finding motivates Eliashberg theory which can be seen as RPA for both the fermion and the boson, i.e. a self-consistent generalization of RPA.

Another method one wishes to exploit is the so called large N or $1/N$ expansion. As the name already suggests, it is an expansion of correlators in powers of $1/N$ with N being the number of fermion flavors. If the method is applicable, it is nothing else than simply

counting the number of vertices n_V and the number of fermion loops n_L in a diagram contributing to the correlation function of interest. Since each (potentially rescaled) vertex contributes by a factor of $1/\sqrt{N}$ and each fermion loop by a factor of N , the whole diagram scales with $N^{n_L - n_V/2}$. Therefore, only diagrams of order $\mathcal{O}(1)$ survive in the limit $N \rightarrow \infty$. It turned out that counting in this way is not always applicable, since so called enhancement factors arise for certain models. They arise due to necessary self-energy corrections which have to be included in the action to cure infrared divergencies. Their consequences are additional counting rules which prohibit a simple expansion. This has been first shown for a single Fermi surface patch by Lee [11] and been extended to a pair of patches by Metlitski and Sachdev [12].

It turned out that renormalization group (RG) treatments are promising methods to deal with the aforementioned actions. As an example, we want to mention the recently performed study by Halbinger, Pimenov and Punk using dimensional regularization and the minimal subtraction scheme [16]. Apart from great results like the confirmation of a second order phase transition or the observed Fermi surface flattening at the hot spots, such one-loop calculations always have to be taken with a grain of salt, since it is not clear if they provide qualitative correct results. It is – as usual – advisable to double check with other methods when interested for instance in the precise values of critical exponents. Note that Eliashberg theory is a promising candidate for this, since it includes arbitrary high loop orders and moreover provides a canonical numerical realization as we will see in Section 2.5. However, notice that the above mentioned ε -expansion is in principle controlled if the extrapolation to $\varepsilon = 1/2$ (or $\varepsilon = 1$) works [16, 33], whereas Eliashberg theory is unfortunately an uncontrolled technique [19–21, 34] which we will comment on in the following chapter.

2.4. Eliashberg Theory

Shortly after BCS theory has been proposed, Migdal and Eliashberg developed a theory generalizing the former to the strong-coupling regime [17, 18]. Although this so called Eliashberg theory was specifically developed in the context of electron-phonon superconductivity it turned out to be a very useful framework for studying many other (strongly coupled) systems in various areas of condensed matter physics [19–21, 34]. The goal of this thesis is to use such an Eliashberg approach to numerically analyze the theory (2.1) and analytically investigate the corresponding hot spot theory (2.6).

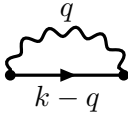
Let us focus on the full theory (2.1) and take a look at the electronic self-energy Σ as well as the polarization Π . These self-energies are of course related to the fermionic and

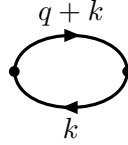
bosonic propagators G and D by the Dyson equations [35]

$$G^{-1}(k) = i\omega_n - \xi_{\mathbf{k}} - \Sigma(k) \quad (2.8)$$

$$D^{-1}(q) = \chi_q^{-1} - \Pi(q) \quad (2.9)$$

again using the abbreviations $k := (\mathbf{k}, \omega_n)$ and $q := (\mathbf{q}, \Omega_n)$. Eliashberg theory now tells us to compute both self-energies in a one-loop fashion however using dressed instead of bare propagators resulting in a set of two coupled, self-consistent, functional equations which read [19–21]

$$\Sigma(k) = \frac{\lambda^2}{\beta V} \sum_q G(k-q)D(q) = \text{diagram} \quad (2.10)$$


$$\Pi(q) = -2 \frac{\lambda^2}{\beta V} \sum_k G(q+k)G(k) = \text{diagram} \quad (2.11)$$


First note that the expression for the polarization contains a factor of 2 due the spin and that the bold lines represent the dressed propagators. Furthermore notice that due to the self-consistency and coupling the Eliashberg equations reveal a “generalized RPA” structure and therefore go beyond standard RPA treatments. In fact, this approach includes all one particle irreducible diagrams neglecting those which would lead to vertex corrections.

Oftentimes, the Eliashberg Eqs. (2.10) and (2.11) are easier to handle in an retarded form. To obtain these equations one rewrites the Matsubara sum as a contour integral followed by an analytic continuation $i\omega_n \rightarrow \omega + i0^+$ to real frequencies. Exploiting standard relations of correlation functions as well as taking the imaginary part, one arrives at [20]

$$\text{Im } \Sigma_{\text{R}}(\mathbf{k}, \omega) = \lambda^2 \int_{\mathbf{q}} \int_{-\infty}^{\infty} \frac{dz}{\pi} (n_{\text{B}}(z) + n_{\text{F}}(z - \omega)) \cdot \text{Im } G_{\text{R}}(\mathbf{k} - \mathbf{q}, \omega - z) \text{Im } D_{\text{R}}(\mathbf{q}, z) \quad (2.12)$$

$$\text{Im } \Pi_{\text{R}}(\mathbf{k}, \Omega) = 2\lambda^2 \int_{\mathbf{q}} \int_{-\infty}^{\infty} \frac{dz}{\pi} (n_{\text{F}}(z) - n_{\text{F}}(z + \Omega)) \cdot \text{Im } G_{\text{R}}(\mathbf{k} + \mathbf{q}, \Omega + z) \text{Im } G_{\text{R}}(\mathbf{q}, z) \quad (2.13)$$

where n_{B} and n_{F} denote the Bose and Fermi distribution. Moreover, we use the convention $\int_{\mathbf{q}} := \int \frac{d^2q}{4\pi^2}$ as well as label retarded self-energies and propagators by the subscript “R”. The explicit derivation of these retarded Eliashberg equations can be found in Appendix A.1. Note that due to the Kramers-Kronig relations we have not lost any

information compared to the imaginary time version of the Eliashberg equations [36].

Let us now turn to the validity of this approach or phrasing it more precisely: When are we allowed to neglect vertex corrections? The original Migdal-Eliashberg theory was developed as a controlled approximation relying on the smallness of the ratio $\lambda\theta_D/E_F$ where θ_D denotes the Debye temperature and E_F the Fermi energy [18]. Unfortunately in most cases such a limit in which Eliashberg theory becomes exact is not known and even unclear if it exists. Meaning for now we are left with an uncontrolled approximation.

A bright spot might be provided by the following argument [19, 37]. Consider the one-loop vertex correction (using dressed propagators) shown in Fig. 2.5a. Setting $k = (-\frac{Q}{2}, 0)$ and $q = (Q, 0)$ gives the contribution scattering on-shell onto the two hot spots at $\pm\frac{Q}{2}$. We expect the dominant contribution to the momentum integral coming from momenta $p \approx \pm Q$. In both cases one fermion will be close to a hot spot while the other one will be far away from both hot spots (see Fig. 2.5b). This however means that we have always at least one internal fermion being highly off-shell, since there is only one frequency to vary/ integrate over. Hence, we expect the whole one-loop vertex correction to be suppressed. Note that this argument is independent of the coupling constant and for this reason also applicable in the strong coupling regime. Furthermore, notice that the reasoning only works due to the presence of the nesting vector Q . When dealing with ordering wave vectors that are no nesting vectors one has to come up with other justifications [20, 21, 34].

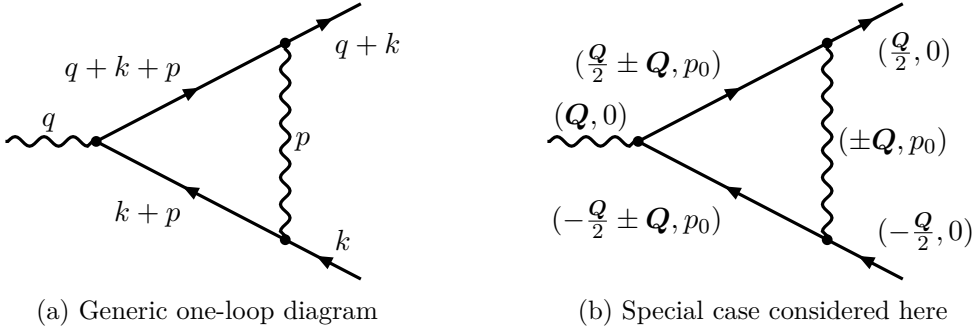


Figure 2.5.: Leading order vertex correction. The bold straight lines depict full fermion propagators, the bold wiggly lines visualize the boson propagator and the points represent bare vertices.

2.5. Iterative Solution

The self-consistent and coupled structure of the Eliashberg equations (2.12) and (2.13) provides a canonical way to numerically solve these equations. This iteration scheme is depicted in Fig. 2.6 and works as follows. One starts with vanishing self-energies $\Sigma_R^{(0)}$

and $\Pi_{\text{R}}^{(0)}$ defined on a $2 + 1$ dimensional grid or to be more precise with vanishing real parts and slightly non-zero imaginary parts to avoid divergencies. As a first step one calculates¹ the imaginary part of the polarization following Eq. (2.13) using (essentially) bare fermionic propagators. Next, one makes use of the Kramers-Kronig relation² [36]

$$\text{Re } \Pi_{\text{R}}^{(1)}(\mathbf{k}, \omega) = \frac{1}{\pi} \mathcal{P} \int_{-\infty}^{\infty} d\omega' \frac{\text{Im } \Pi_{\text{R}}^{(1)}(\mathbf{k}, \omega')}{\omega' - \omega} \quad (2.14)$$

and arrives at the one-loop hence RPA polarization $\Pi_{\text{R}}^{(1)}$. Using the Eliashberg equation (2.12) together with $\Pi_{\text{R}}^{(1)}$ and $\Sigma_{\text{R}}^{(0)}$ we are able to compute the imaginary part of the self-energy $\Sigma_{\text{R}}^{(1)}$. Exploiting Kramers-Kronig relation again we end up with the complete fermionic self-energy $\Sigma_{\text{R}}^{(1)}$, thus having completed one loop. By repeating this scheme one goes beyond RPA and stops when (sufficient) convergence is reached. With other words, one repeats this procedure until being sufficiently close to the fixed point living in the product space of the self-energy function spaces.



Figure 2.6.: Scheme used to find the numerical solution of the Eliashberg equations (2.12) and (2.13). Knowing $\Sigma_{\text{R}}^{(n-1)}$ being the self-energy of the $(n - 1)^{\text{th}}$ self-consistency loop one is able calculate the polarization $\Pi_{\text{R}}^{(n)}$ of the following loop. As the second step in the n^{th} self-consistency loop one now computes self-energy $\Sigma_{\text{R}}^{(n)}$ using both $\Sigma_{\text{R}}^{(n-1)}$ and $\Pi_{\text{R}}^{(n)}$. This was one self-consistency loop and the procedure is done until convergence is reached starting from (almost) vanishing self-energies.

¹We use the so called VEGAS Algorithm which is an adaptive Monte Carlo integrator.

²For example using the adaptive GSL integrator for principle value integrals.

3. Biconvex Geometries

The goal of this chapter is to analytically investigate the hot spot theory (2.6) for a biconvex Fermi patch geometry as depicted in Fig. 2.3. We will therefore be using the dispersion relation (2.4) throughout this chapter. Note that the corresponding numerical treatment will be presented in the subsequent Chapter 4.

3.1. Scattering Rate

Let us first analyze the fermionic self-energy by investigating the corresponding Eliashberg equation. In principle we have two of those equations to solve, since our theory contains two hot spots. However, due to the presence of inversion symmetry it is sufficient to study only one of these equations. One may for example analyze the self-energy for fermions living close to the + hot spot, hence we consider

$$\Sigma_+(k) = \frac{\lambda^2}{\beta V} \sum_q G_-(k-q) D_+(q) \quad (3.1)$$

where again G_- and D_+ are fermionic and bosonic propagators with appropriate hot spot labels and the abbreviations $k := (\mathbf{k}, \omega_n)$ and $q := (\mathbf{q}, \Omega_n)$ were exploited. Since one sums over bosonic Matsubara frequencies we are able to split the self-energy into a classical part $\Sigma_+^{(\text{cl})}$ (coming from the frequency $\Omega_0 = 0$) and a quantum part $\Sigma_+^{(\text{qu})}$ (arising from all frequencies $\Omega_{n \neq 0}$). Note that the classical part only contributes for $T > 0$, since at $T = 0$ it becomes a null set [20]. Let us first focus on the classical part given by

$$\Sigma_+^{(\text{cl})}(\mathbf{k}, i\omega_n) = \frac{\lambda^2}{\beta V} \sum_q G_-(\mathbf{k} - \mathbf{q}, i\omega_n) D_+(\mathbf{q}, 0). \quad (3.2)$$

Due to the self-consistency and non-linearity this is still too complicated to be calculated in general. However, one is able to derive an explicit expression for the classical scattering

rate

$$\gamma_+^{(\text{cl})} := -\text{Im} \Sigma_+^{(\text{cl})}(\mathbf{0}, 0) \quad (3.3)$$

$$= \frac{\lambda^2}{\beta V} \sum_{\mathbf{q}} \frac{-\text{Im} \Sigma_+(\mathbf{q}, 0)}{\xi_{+,\mathbf{q}}^2 + (\text{Im} \Sigma_+(\mathbf{q}, 0))^2} \cdot \frac{1}{m + A\mathbf{q}^2} . \quad (3.4)$$

Note that we neglected the real part of the fermion self-energy for simplicity. Also notice that we have taken the real part of the polarization, at least to some extent, into account, since the renormalized mass m and the quadratic term $A\mathbf{q}^2$ stem from a low-energy expansion of the polarization's real part. Moreover, note that the imaginary part drops out in our classical consideration which can be seen by the Eliashberg equation (2.13) when setting the external frequency to zero. For low enough temperatures we expect the main contribution to be

$$\gamma_+^{(\text{cl})} = \frac{\lambda^2}{\beta V} \sum_{\mathbf{q}} \frac{\gamma_+}{\xi_{+,\mathbf{q}}^2 + \gamma_+^2} \cdot \frac{1}{m + A\mathbf{q}^2} . \quad (3.5)$$

Inserting the explicit form of the dispersion relation as well as substituting $\mathbf{k} := \sqrt{A/m} \cdot \mathbf{q}$ we arrive at the expression

$$\gamma_+^{(\text{cl})} = \frac{\lambda^2}{4\pi^2 \beta \gamma_+ A} \int d^2 k \frac{1}{(ak_x + bk_y^2)^2 + 1} \cdot \frac{1}{1 + k_x^2 + k_y^2} \quad (3.6)$$

containing the two parameters $a := \frac{v_F \sqrt{m}}{\gamma_+ \sqrt{A}} > 0$ and $b := \frac{\kappa m}{2\gamma_+ \sqrt{A}} > 0$. Even if this integral looks relatively harmless, it unfortunately is quite a complex object due to the two parameters. We will therefore try to find the dominant contribution by applying the subsequent scaling argument. Consider the hot spot action (2.6) or to be more precise the purely fermionic part which suggests the following rescalings after having performed a “decimation” step in a momentum shell RG program:

$$k'_x = b^2 \cdot k_x \quad (3.7)$$

$$k'_y = b \cdot k_y . \quad (3.8)$$

Hence the term Aq_x^2 in the Eqs. (2.5) and (2.6) is irrelevant in the low-energy limit. We therefore proceed with

$$\gamma_+^{(\text{cl})} = \frac{\lambda^2}{4\pi^2 \beta \gamma_+ A} \int d^2 k \frac{1}{(ak_x + bk_y^2)^2 + 1} \cdot \frac{1}{1 + k_y^2} \quad (3.9)$$

$$= \frac{\lambda^2}{4\pi^2 \beta \gamma_+ A} \int dk_y \frac{\pi}{a \cdot (1 + k_y^2)} \quad (3.10)$$

$$= \frac{\lambda^2}{4\beta \gamma_+ A a} . \quad (3.11)$$

Inserting the above defined parameter a back into the derived expression gives the final result for the classical scattering rate

$$\gamma_+^{(\text{cl})} = \frac{\lambda^2}{4v_F\sqrt{A}} \frac{T}{\sqrt{m(T)}} \quad (3.12)$$

Note that the parameter b has dropped out earlier and for this reason our result may look curvature-independent. However, there is still the chance that the mass depends on the curvature κ which would restore the curvature-dependence of the scattering rate $\gamma_+^{(\text{cl})}$. Moreover notice that our result turned out to be extremely similar to the one obtained by Punk in the context of Ising-nematic order [20].

The good news is that we were able to derive an analytic expression for the classical part of the scattering rate. As already pointed out we are not done yet, since the formula still depends on the renormalized mass which is so far unknown. For this reason we try to derive an analytic expression in the following section.

3.2. Renormalized Mass

From Section 2.2 we recall that the gap or renormalized mass $m(T)$ at a certain temperature T is given by

$$m(T) = \text{Re } \Pi_{+,R}(\mathbf{0}, 0, T = 0) - \text{Re } \Pi_{+,R}(\mathbf{0}, 0, T) \quad (3.13)$$

meaning this section will be all about calculating polarizations at zero momentum and frequency. For this, one may use the retarded version of the Eliashberg equation for the real part of the polarization which of course looks quite similar to the retarded Eliashberg equation (2.13) for the imaginary part, since the derivations are essentially the same. In the hot spot version the former reads

$$\begin{aligned} \text{Re } \Pi_{+,R}(\mathbf{k}, \Omega) = 2\lambda^2 \int_{\mathbf{q}} \int_{-\infty}^{\infty} \frac{dz}{\pi} n_F(z) & \left(\text{Re } G_{+,R}(\mathbf{k} + \mathbf{q}, \Omega + z) \text{Im } G_{-,R}(\mathbf{q}, z) \right. \\ & \left. + \text{Re } G_{-,R}(\mathbf{q}, z - \Omega) \text{Im } G_{+,R}(\mathbf{k} + \mathbf{q}, z) \right) \end{aligned} \quad (3.14)$$

Exploiting $G_{+,R}(\mathbf{k}, \omega) = G_{-,R}(-\mathbf{k}, \omega)$ and setting the external momentum and frequency to zero we arrive at the slightly simpler form

$$\text{Re } \Pi_{+,R}(\mathbf{0}, 0) = 4\lambda^2 \int_{\mathbf{q}} \int_{-\infty}^{\infty} \frac{dz}{\pi} n_F(z) \text{Re } G_{+,R}(\mathbf{q}, z) \text{Im } G_{+,R}(-\mathbf{q}, z). \quad (3.15)$$

Before considering Eliashberg theory let us first take a look at the RPA. Hence we

compute the bare bubble and therefore we use the equation above with only bare fermion propagators. This leads to

$$\text{Re } \Pi_{+,R}^{(\text{RPA})}(\mathbf{0}, 0) = 4\lambda^2 \int_{\mathbf{q}} \int_{-\infty}^{\infty} \frac{dz}{\pi} n_{\text{F}}(z) \cdot \frac{1}{z - \xi_{+, \mathbf{q}}} \cdot (-\pi) \delta(z - \xi_{+, -\mathbf{q}}) \quad (3.16)$$

$$= -\frac{\lambda^2}{2\pi^2} \int d^2q \frac{n_{\text{F}}(v_{\text{F}}q_x + \frac{\kappa}{2}q_y)}{v_{\text{F}}q_x} \quad (3.17)$$

$$= -\frac{\lambda^2}{\sqrt{2\kappa}\pi^2 v_{\text{F}}} \int d^2k \frac{1}{k_x} \cdot \frac{1}{\exp(\beta(k_x + k_y^2)) + 1} \quad (3.18)$$

where we inserted the explicit expression for the dispersion relation (2.4). A substitution as $k_x \rightarrow k_x/\beta$ and $k_y \rightarrow k_y/\sqrt{\beta}$ already shows that we can expect the mass to scale as $m^{(\text{RPA})} \sim 1/\sqrt{\beta} = \sqrt{T}$. To obtain the prefactors one has to renormalize, since the above integral diverges and of course solve the integrals. This calculation is provided in Appendix A.2 and leads to the following final result for the boson mass in RPA

$$m^{(\text{RPA})}(T) = \frac{\lambda^2 c}{\sqrt{2\kappa}\beta\pi^2 v_{\text{F}}} \sim \sqrt{T} \quad (3.19)$$

which $c \approx 3.37$ being a numerical constant.

Let us now try to derive an analogue expression in Eliashberg theory and see in particular if the critical exponent of 1/2 changes. Again we start from Eq. (3.15) by inserting the expressions for the propagators which gives

$$\text{Re } \Pi_{+,R}(\mathbf{0}, 0) = 4\lambda^2 \int_{\mathbf{q}} \int_{-\infty}^{\infty} \frac{dz}{\pi} n_{\text{F}}(z) \cdot \frac{z - \xi_{+, \mathbf{q}}}{(z - \xi_{+, \mathbf{q}})^2 + (\text{Im } \Sigma_{+,R}(\mathbf{q}, z))^2} \cdot \frac{\text{Im } \Sigma_{+,R}(-\mathbf{q}, z)}{(z - \xi_{+, -\mathbf{q}})^2 + (\text{Im } \Sigma_{+,R}(-\mathbf{q}, z))^2} \cdot \quad (3.20)$$

Since we expect the dominant contribution to the integral to come from the Fermi surface, we estimate

$$\text{Re } \Pi_{+,R}(\mathbf{0}, 0) = 4\lambda^2 \int_{\mathbf{q}} \int_{-\infty}^{\infty} \frac{dz}{\pi} n_{\text{F}}(z) \cdot \frac{z - \xi_{+, \mathbf{q}}}{(z - \xi_{+, \mathbf{q}})^2 + \gamma_+^2} \cdot \frac{-\gamma_+}{(z - \xi_{+, -\mathbf{q}})^2 + \gamma_+^2} \cdot \quad (3.21)$$

Unfortunately this expression is still too complicated to be solved analytically. Since we are mainly interested in the temperature-dependence, we wish to find at least the leading order term with respect to the temperature. This is for example possible by performing a Sommerfeld expansion which will be given in the following Section 3.3. Using the result in advance, the leading order temperature dependence comes from

$$\text{Re } \Pi_{+,R}(\mathbf{0}, 0) = 4\lambda^2 \int_{\mathbf{q}} \int_{-\infty}^0 \frac{dz}{\pi} \frac{z - \xi_{+, \mathbf{q}}}{(z - \xi_{+, \mathbf{q}})^2 + \gamma_+^2} \cdot \frac{-\gamma_+}{(z - \xi_{+, -\mathbf{q}})^2 + \gamma_+^2} \cdot \quad (3.22)$$

Now that we got rid of the Fermi distribution it is possible to apply the substitutions $z \rightarrow \gamma_+ z$, $q_x \rightarrow \gamma_+ q_x$ and $q_y \rightarrow \sqrt{\gamma_+} q_y$ already showing $m \sim \sqrt{\gamma_+}$. The explicit calculation involving all the prefactors is provided in Appendix A.3 and leads to the following result:

$$m(T) = \frac{2\lambda^2}{\sqrt{\kappa}\pi v_F} \sqrt{\gamma_+(T)} \quad (3.23)$$

Since the derived mass term depends on the scattering rate and vice versa (Eq. (3.12)), it is tempting to directly solve for both. As we will see shortly, one needs to be a little more careful, since the expression for the mass (Eq. (3.23)) depends on the full scattering rate while Eq. (3.12) provides only a formula for the classical scattering rate. We therefore proceed by only plugging the expression for the mass into the formula for the classical scattering rate which yields

$$\gamma_+^{(\text{cl})}(T) \sim \frac{T}{\sqrt[4]{\gamma_+(T)}} = \frac{T}{\sqrt[4]{\gamma_+^{(\text{cl})}(T) + \gamma_+^{(\text{qu})}(T)}}. \quad (3.24)$$

Assume for now that the quantum part $\gamma_+^{(\text{qu})}$ is subleading for low enough temperatures compared to the classical part. Hence we find

$$\gamma_+^{(\text{cl})}(T) \sim \frac{T}{\sqrt[4]{\gamma_+^{(\text{cl})}(T)}} \quad (3.25)$$

$$\Rightarrow \gamma_+^{(\text{cl})}(T) \sim T^{4/5}. \quad (3.26)$$

Let us now turn to the quantum part to see if our assumption holds. We may estimate this part by using the zero temperature RPA result obtained by Sýkora, Holder and Metzner [13] and exploiting ω/T -scaling. Hence we expect

$$\gamma_+^{(\text{qu})}(T) \sim T^{2/3} \quad (3.27)$$

which clearly shows that our assumption of a subleading quantum part was wrong and therefore conclude that the classical scattering rate is subleading for sufficiently small temperatures. We would like to point out that this behavior clearly differs from the one found in metals close to Ising-nematic quantum critical points [20], since there classical fluctuations provided the leading order term due to a different mass scaling ($\sim \sqrt{T} |\ln T|$ [38]). Speaking of the mass – how does it scale now? Plugging the relation (3.27) into

Eq. (3.23) gives us the answer:

$$m(T) \sim T^{1/3} \quad (3.28)$$

Notice that the critical exponent relating the mass to the temperature has dropped from 1/2 to 1/3 going (at least somewhat) beyond RPA. This is in contrast to the RG studies for this model performed by Halbinger, Pimenov and Punk [16] since they found an exponent of 0.616. Note that neglected vertex corrections do not qualify as a possible explanation for this discrepancy, since the vertex does not renormalize in one-loop RG due to the same ‘‘momentum argument’’ as provided in Section 2.4 for Eliashberg theory. Possible explanations are however the one-loop structure of their RG study or on the Eliashberg side the plenty approximations we used to derive this result.

Notice that we are now also able to calculate the correct scaling of the (subleading) classical fluctuations by simply plugging the relation (3.28) into the earlier found expression (3.12)

$$\gamma_+^{(\text{cl})}(T) \sim T^{5/6} \quad (3.29)$$

3.3. Sommerfeld Expansion

Having derived and discussed all the results above, let us not forget that we still have to justify the step of calculation from Eq. (3.21) to Eq. (3.22). Especially since we were interested in the temperature dependence of the mass, the approximation $n_{\text{F}}(z) \approx \theta(z)$ seems questionable. The aim of this section is to resolve this by a Sommerfeld expansion. Since a lot of real constants will appear in this section, we will simply denote them by a ‘‘ \mathbb{R} ’’. Let us start by stating Eq. 3.21 again

$$\text{Re } \Pi_{+, \text{R}}(\mathbf{0}, 0) = \frac{4\lambda^2}{\pi} \int_{\mathbf{q}} \int_{-\infty}^{\infty} dz n_{\text{F}}(z) \cdot f_{\mathbf{q}}(z) \quad (3.30)$$

where we used the abbreviation

$$f_{\mathbf{q}}(z) := \frac{z - \xi_{+, \mathbf{q}}}{(z - \xi_{+, \mathbf{q}})^2 + \gamma_+^2} \cdot \frac{-\gamma_+}{(z - \xi_{+, -\mathbf{q}})^2 + \gamma_+^2}. \quad (3.31)$$

Performing the promised Sommerfeld expansion yields

$$\text{Re } \Pi_{+, \text{R}}(\mathbf{0}, 0) = \frac{4\lambda^2}{\pi} \int_{\mathbf{q}} \left(\int_{-\infty}^0 dz f_{\mathbf{q}}(z) + \sum_{n=1}^{\infty} \mathbb{R} \cdot T^{2n} \cdot \left. \frac{d^{2n-1} f_{\mathbf{q}}(z)}{dz^{2n-1}} \right|_{z=0} \right). \quad (3.32)$$

Note that the first summand is exactly the one we worked with in the last section and therefore Eq. (3.23) tells us

$$\text{Re } \delta\Pi_{+,R}(\mathbf{0}, 0) = \mathbb{R}\sqrt{\gamma_+} + \int_{\mathbf{q}} \sum_{n=1}^{\infty} \mathbb{R} \cdot T^{2n} \cdot \left. \frac{d^{2n-1} f_{\mathbf{q}}(z)}{dz^{2n-1}} \right|_{z=0} \quad (3.33)$$

where we already removed the divergence by simply subtracting the zero temperature limit, meaning we consider the renormalized polarization $\delta\Pi_{+,R}$ here. It turns out to be quite useful to substitute $k_x := q_x/\gamma_+$ and $k_y := q_x/\sqrt{\gamma_+}$ resulting in

$$\text{Re } \delta\Pi_{+,R}(\mathbf{0}, 0) = \mathbb{R}\sqrt{\gamma_+} + \int_{\mathbf{k}} \gamma_+^{3/2} \sum_{n=1}^{\infty} \mathbb{R} \cdot T^{2n} \cdot \left. \frac{d^{2n-1} f_{(\gamma_+ k_x, \sqrt{\gamma_+} k_y)}(z)}{dz^{2n-1}} \right|_{z=0}. \quad (3.34)$$

Now our task is to find out how the derivatives depend on $\gamma_+(T)$. Since this is rather technical but straight forward, we perform this calculation in Appendix A.4 and state here only the result

$$\left. \frac{d^{2n-1} f_{(\gamma_+ k_x, \sqrt{\gamma_+} k_y)}(z)}{dz^{2n-1}} \right|_{z=0} = h(\mathbf{k}) \cdot \gamma_+^{-2n-1} \quad (3.35)$$

where h is a momentum-dependent function specified in the appendix as well. Plugging this expression in the above equation for the renormalized polarization yields

$$\text{Re } \delta\Pi_{+,R}(\mathbf{0}, 0) = \mathbb{R}\sqrt{\gamma_+} + \sum_{n=1}^{\infty} \mathbb{R} \cdot T^{2n} \cdot \gamma_+^{-2n+\frac{1}{2}} \quad (3.36)$$

$$= \sqrt{\gamma_+} \cdot \sum_{n=0}^{\infty} \mathbb{R} \cdot \left(\frac{T}{\gamma_+} \right)^{2n}. \quad (3.37)$$

Assuming $\gamma_+ \sim T^\alpha$ with $\alpha \in (0, \infty)$ gives

$$\text{Re } \delta\Pi_{+,R}(\mathbf{0}, 0) = T^{\frac{\alpha}{2}} \sum_{n=0}^{\infty} \mathbb{R} \cdot T^{2n(1-\alpha)} \quad (3.38)$$

which tells us that the approximation in the last chapter is valid for $(1 - \alpha) \geq 0$. Thus we find a region of validity of $0 < \alpha \leq 1$. Since the previously determined exponent of $2/3$ (Eq. (3.27)) lies within this region, we can view this Sommerfeld expansion as a posteriori justification of the approximation in the last section.

3.4. Imaginary Part of Polarization

The last quantity we want to analytically calculate in the biconvex geometry is the imaginary part of the polarization. Besides being an interesting object itself, it also provides two dynamical critical exponents which will tell us how the Fermi surface close

to the hot spots renormalizes as we will see later on. Let us start from the hot spot analogue of Eq. (2.13)

$$\begin{aligned} \text{Im } \Pi_{+,R}(\mathbf{k}, \Omega) &= 2\lambda^2 \int_{\mathbf{q}} \int_{-\infty}^{\infty} \frac{dz}{\pi} (n_F(z) - n_F(z + \Omega)) \\ &\quad \cdot \text{Im } G_{+,R}(\mathbf{k} + \mathbf{q}, \Omega + z) \text{Im } G_{-,R}(\mathbf{q}, z). \end{aligned} \quad (3.39)$$

For small enough external frequencies we may expand the second Fermi distribution up to linear order in Ω , hence

$$n_F(z) - n_F(z + \Omega) \simeq -\frac{\partial n_F(z)}{\partial z} \cdot \Omega \quad (3.40)$$

$$\simeq \delta(z) \cdot \Omega \quad (3.41)$$

where the second step becomes exact in the zero temperature limit. Therefore, we arrive at

$$\text{Im } \Pi_{+,R}(\mathbf{k}, \Omega) = \frac{2\lambda^2\Omega}{\pi} \int_{\mathbf{q}} \text{Im } G_{+,R}(\mathbf{k} + \mathbf{q}, 0) \text{Im } G_{-,R}(\mathbf{q}, 0). \quad (3.42)$$

Inserting the explicit expressions and approximating one Lorentzian by a delta distribution gives

$$\text{Im } \Pi_{+,R}(\mathbf{k}, \Omega) = 2\lambda^2\Omega \int_{\mathbf{q}} \frac{-\text{Im } \Sigma_{+,R}(\mathbf{k} + \mathbf{q}, 0)}{(\xi_{+, \mathbf{k} + \mathbf{q}})^2 + (\text{Im } \Sigma_{+,R}(\mathbf{k} + \mathbf{q}, 0))^2} \cdot \delta(\xi_{-, \mathbf{q}}). \quad (3.43)$$

For small external momenta we may further approximate

$$\text{Im } \Pi_{+,R}(\mathbf{k}, \Omega) = 2\lambda^2\Omega \int_{\mathbf{q}} \frac{\gamma_+}{(\xi_{+, \mathbf{k} + \mathbf{q}})^2 + \gamma_+^2} \cdot \delta(\xi_{-, \mathbf{q}}) \quad (3.44)$$

$$= \frac{\lambda^2\Omega}{2\pi^2 v_F \sqrt{\kappa\gamma_+}} \int_{-\infty}^{\infty} dx \frac{1}{(x^2 + e_{\mathbf{k}}/\gamma_+)^2 + 1} \quad (3.45)$$

$$= \frac{\lambda^2\Omega}{2\pi^2 v_F \sqrt{\kappa\gamma_+}} \cdot \frac{i\pi}{2} \left(\frac{1}{\sqrt{e_{\mathbf{k}}/\gamma_+ + i}} - \frac{1}{\sqrt{e_{\mathbf{k}}/\gamma_+ - i}} \right) \quad (3.46)$$

where we defined $e_{\mathbf{k}} := v_F k_x + \frac{\kappa}{4} k_y^2$. Getting rid of the complex roots we arrive at the final expression

$$\text{Im } \Pi_{+,R}(\mathbf{k}, \Omega) = \frac{\lambda^2\Omega}{2\pi v_F \sqrt{2\kappa}} \cdot \frac{\sqrt{\sqrt{e_{\mathbf{k}}^2 + \gamma_+^2} - e_{\mathbf{k}}}}{\sqrt{e_{\mathbf{k}}^2 + \gamma_+^2}} \quad (3.47)$$

which immediately reminds of the RPA result obtained by Sýkora, Holder and Metzner [13, 14]. Let us try to build some intuition for this formula by looking at different limits.

First, consider the zero temperature limit ($\gamma_+ \rightarrow 0$)

$$\text{Im } \Pi_{+,R}(\mathbf{k}, \Omega, T = 0) = \frac{\lambda^2}{2\pi v_F \sqrt{\kappa}} \cdot \frac{\Omega \cdot \theta(-e_{\mathbf{k}})}{\sqrt{|e_{\mathbf{k}}|}} \quad (3.48)$$

which can be used to derive the aforementioned dynamical critical exponents. For instance to determine the exponent orthogonal to the Fermi surface one sets $k_y = 0$ in the formula above, applies the rescalings $k'_x = bk_x$ and $\Omega' = b^{z_\perp} \Omega$ and fixes the missing exponent by matching scaling dimensions with the Ornstein-Zernike term (2.5). We therefore conclude $z_\perp = 5/2$. Analogously we find parallel to the Fermi surface a dynamical critical exponent $z_\parallel = 3$. Therefore, we expect the renormalized Fermi surface close to the hot spots to be of the form $k_x \sim |k_y|^{2z_\parallel/z_\perp} = |k_y|^{12/5}$ meaning we find dynamical nesting, in qualitative accordance to Halbinger, Pimenov and Punk since they found an exponent of 3.85 [16]. This finding is visualized in Fig. 3.1 again.

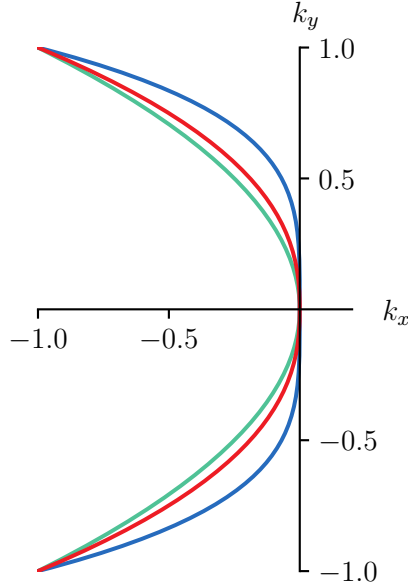


Figure 3.1.: Comparison of different (low-energy) Fermi surfaces located at the right hot spot. While the green lines depicts the non-interacting Fermi surface, the red line shows the interacting one obtained by Eliashberg theory. In both cases we set $v_F = 1$ and $\kappa = 2$ for simplicity. The blue line shows the corresponding renormalized Fermi surface found by Halbinger, Pimenov and Punk using the aforementioned RG approach [16].

Finally, consider the case of vanishing external momenta

$$\text{Im } \Pi_{+,R}(\mathbf{0}, \Omega) = \frac{\lambda^2}{2\pi v_F \sqrt{2\kappa}} \cdot \frac{\Omega}{\sqrt{\gamma_+}}. \quad (3.49)$$

We observe that the term $\sim \frac{\Omega}{\sqrt{|e_{\mathbf{k}}|}}$ in Eq. (3.48) transforms into a quite similar look-

ing term $\sim \frac{\Omega}{\sqrt{\gamma_+}}$ when turning from the zero temperature limit to the regime of finite temperature but zero external momenta. This behavior reminds us of the Eliashberg approach by Punk [20] for metals close to an Ising-nematic quantum critical point where the Landau damping term $\sim \frac{\Omega}{|k|}$ turned into a term $\sim \frac{\Omega}{\gamma}$.

4. Tight Binding Model

Let us now turn to the numerical solution of the Eliashberg equations (2.12) and (2.13) by exploiting the iterative algorithm described in Section 2.5. We perform this numerical analysis due to two main reasons. Firstly, our analytical investigations presented in the previous section relied on a couple of approximations. It is therefore always advisable to double-check the results using a different method. Secondly, the analytical calculations are typically only feasible for very specific external momenta or frequencies. The fermionic self-energy $\text{Im } \Sigma_{+,R}$ serves as a perfect example here, since it only has been investigated for zero momentum and frequency, hence solely on-shell on the Fermi surface. It is therefore interesting to study the model also in regions which remain hidden in an analytical Eliashberg treatment.

4.1. Numerical Setup

We want to start off by a few comments on the numerical treatment. The retarded Eliashberg equations will be solved on a square lattice with momenta discretized on a 49×49 equidistant grid in the first Brillouin zone. In frequency space we will use a cubic-spaced grid with 101 (149) sites for $\text{Im } \Sigma_R$, $\text{Re } \Sigma_R$, $\text{Re } \Pi_R$ ($\text{Im } \Pi_R$) up to a maximal frequency of 11 (in units of the below specified nearest neighbor hopping amplitude t) due to small frequencies giving the dominant contributions. As already mentioned before, we choose the tight binding dispersion relation [39]

$$\xi_{\mathbf{k}} = -2t (\cos(k_x) + \cos(k_y)) - 4t' \cos(k_x) \cos(k_y) - \mu \quad (4.1)$$

where we have set the lattice constant to unity, t and t' are the nearest and next nearest neighbor hopping amplitudes and μ denotes the chemical potential. Note that the D_4 symmetry of the chosen dispersion relation reduces the run time by a factor of 8, since it suffices to solve the Eliashberg equations on an octant of the Brillouin zone. Setting $t = 1$ throughout this chapter still leaves us with t' and μ to be chosen. The idea is now to choose them in such a way that the system is likely to develop nesting vectors in nodal direction as depicted in Fig. 4.1. A suitable parameter regime can be typically

found with the help of so called $2k_F$ lines. These are nothing else than the set of all momenta \mathbf{k} fulfilling

$$\xi_{\frac{\mathbf{k}+\mathbf{G}}{2}} = 0 \quad (4.2)$$

for arbitrary reciprocal lattice vectors \mathbf{G} . For an inversion symmetric dispersion relation one therefore finds all vectors which go through the origin and connect two points on the Fermi surface with parallel tangents. In the case of our tight binding dispersion relation one has exactly determined all nesting vectors. How can we now use these $2k_F$ line(s) to choose the parameters t' and μ ? As in Fig. 4.1 we want a relatively small Fermi surface “diameter” such that the $2k_F$ line does not exceed the first Brillouin zone. Note that backfolding would make the situation a lot more complicated, since $2k_F$ line intersections would appear which could lead to even more than the expected four hot spots. We therefore choose the Fermi surface to go through the point $\mathbf{k}_{\text{pin}} = (0.65, 0.65)$. At this point we tune the Fermi surface curvature to zero by setting $t'/t = -0.398$. With these two choices the chemical potential is already determined, reading $\mu/t = -2.175$.

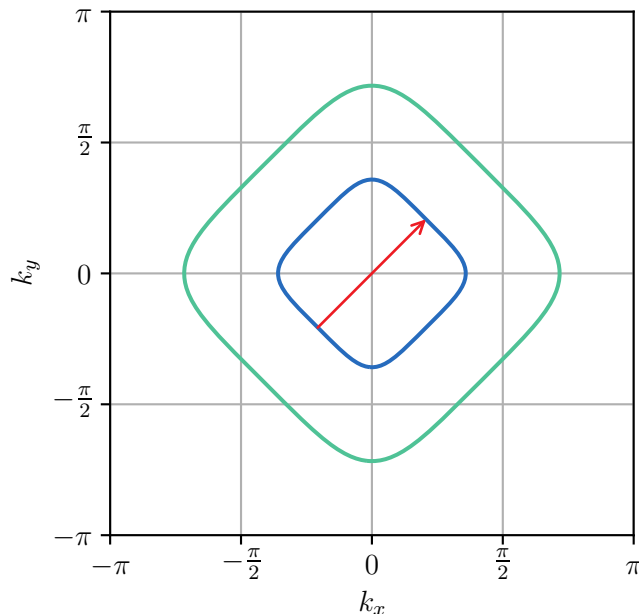


Figure 4.1.: The blue line depicts the Fermi surface arising from the tight binding dispersion relation (4.1) for $t'/t = -0.398$ and $\mu/t = -2.175$. An adequate choice of the next nearest neighbor hopping amplitude leads to vanishing Fermi surface curvature at the nodal points. Note that these two parameters have been chosen such that the $2k_F$ line, depicted in green, lies well within the first Brillouin zone and does not need to be folded back. One of the four hoped-for nesting vectors is shown in red.

Lastly, we set the coupling constant $\lambda/t = 0.7$, choose an inverse temperature $\beta t = 50$

and fix the renormalized mass $m/t = 0.01$, since this seemed like a reasonable choice of parameters compared to similar Eliashberg studies by Punk [19, 20]. Notice that in our numerical calculations we can neither set the mass nor the temperature exactly to zero, since the former would give rise to a pole appearing in the boson propagator and the latter would turn Lorentzians (from $\text{Im } \Sigma_{\text{R}}$) into delta distributions, thus both cases would cause major computational problems. Therefore, we only use a small (compared to t) temperature and renormalized mass. The latter will also be the only term appearing in the bare susceptibility, hence the momentum- and frequency-dependence of the dressed susceptibility will solely arise from the (renormalized) polarization. We will also keep the renormalized chemical potential $\mu_{\text{ren}} := \mu - \text{Re } \Sigma_{\text{R}}(\mathbf{k}_{\text{pin}}, 0)$ instead of the bare chemical potential μ fixed throughout the computations. Thus the Fermi surface will always be pinned to the earlier chosen point \mathbf{k}_{pin} on the Fermi surface which prevents, at least to some extent, strong Fermi surface changes for example due to backfolding.

4.2. Results

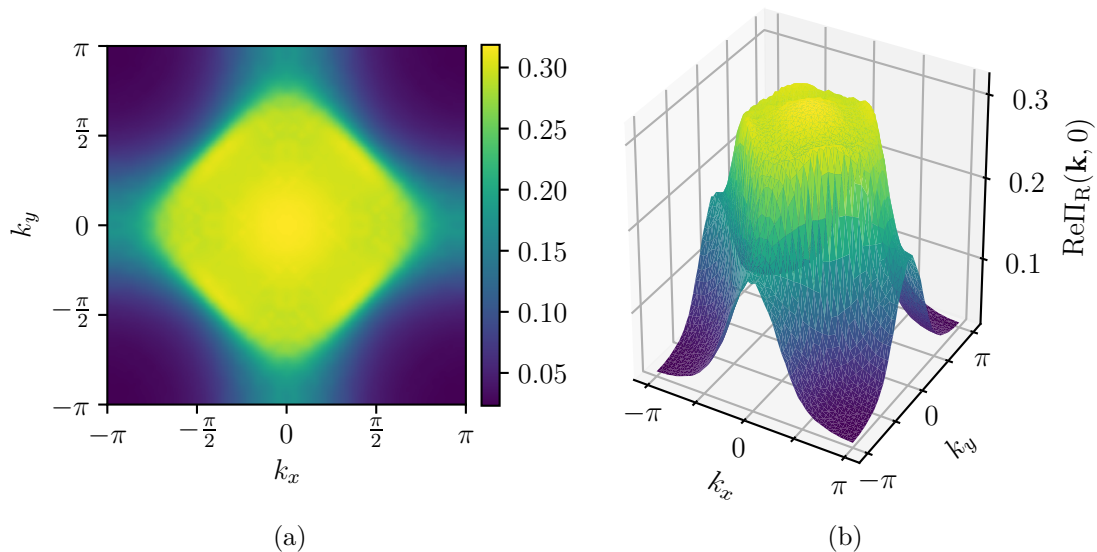


Figure 4.2.: Density (a) and surface (b) plot of the static polarization $\text{Re } \Pi_{\text{R}}(\mathbf{k}, 0)$ after the first loop. We observe the expected but rather small peaks on the diagonals on top of a high unexpected central plateau which also hosts a central peak. Parameters: $\beta t = 50$, $m/t = 0.01$, $\lambda/t = 0.7$, $t'/t = -0.398$, $\mu/t = -2.175$.

Let us dive into the results by checking on the static polarization after one loop which is of course nothing else than the (static) RPA polarization¹. One gains a first impression of the situation by looking at the density and surface plots in Fig. 4.2. We observe a

¹Note, that RPA is clearly not self-consistent! The term “one loop” means only that we have gone once through the for loop on our way to a fully self-consistent solution.

tall, unexpected plateau located at the center of the Brillouin zone. Taking a closer look at the plateau we can already guess its substructure which are five maxima – four in the nodal directions and one at $\mathbf{k} = \mathbf{0}$. While the origin of the latter maximum remains unclear, the former four arise due to the vanishing Fermi surface curvature at the nodal points. A detailed view of these maxima can be obtained by looking at cuts in diagonal and axial direction which are depicted in Fig. 4.3. Analyzing these plots we conclude that the peak right at the origin turns out to be the global maximum.

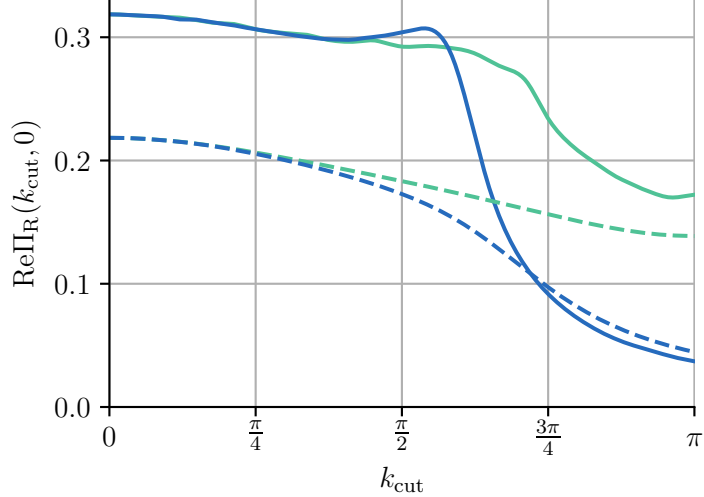


Figure 4.3.: Depicted are various cuts of the static polarization $\text{Re } \Pi_{\text{R}}(\cdot, 0)$ in momentum space. The blue lines correspond to a diagonal direction and we use $k_{\text{cut}} := \sqrt{k_x^2 + k_y^2}$. Moreover, the green lines display the polarization along one of the axes and we use $k_{\text{cut}} := k_x$ and set $k_y = 0$ (or vice versa). Note that the solid lines show the results after one loop and the dashed lines depict the fully converged polarization after 10 loops. Notice that the local maximum at finite wave vector from the first loop is no longer present at higher loop numbers. Same parameters as above: $\beta t = 50$, $m/t = 0.01$, $\lambda/t = 0.7$, $t'/t = -0.398$, $\mu/t = -2.175$.

Next, turn to the scattering rate at Fermi energy and analyze this quantity still after having performed only one loop. The corresponding density and surface plots are shown in Fig. 4.4. One observes large scattering rates on top of the whole Fermi surface. The maxima are clearly located in axial direction which surprises a little, since we expected the hot spots to lie at the nodal points. This behavior is caused by the global maximum of the polarization at $\mathbf{k} = \mathbf{0}$ which might give rise to an enhanced scattering “bridging” the Fermi surface’s corners.

Let us now go beyond RPA, hence look at results at higher loop order. Unfortunately, it turns out that already in second loop order the desired peaks of the polarization at finite wave vectors completely disappear leaving us with an ordering wave vector of $\mathbf{Q} = \mathbf{0}$.

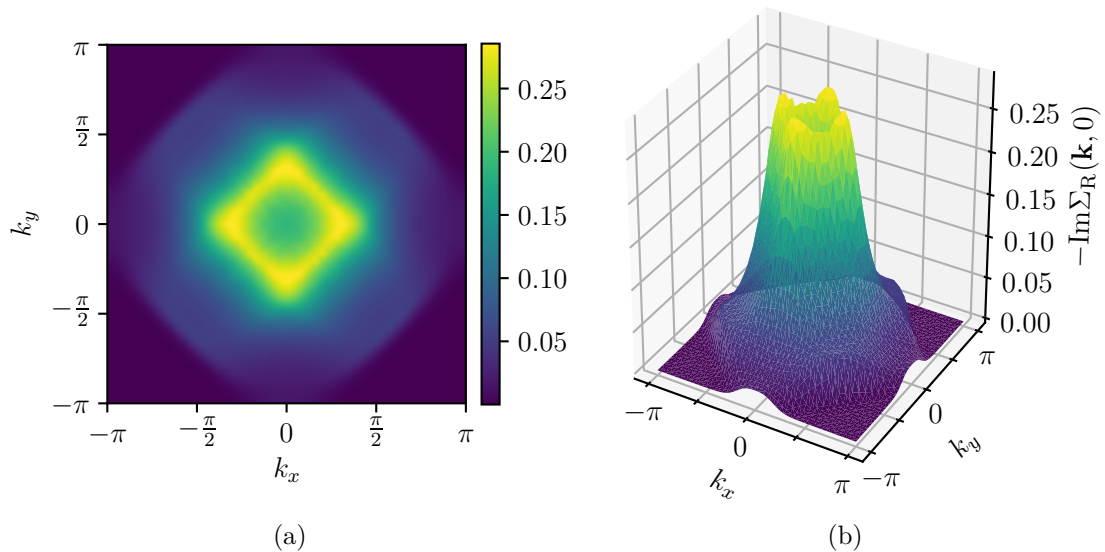


Figure 4.4.: Density (a) and surface (b) plot of the scattering rate $-\text{Im}\Sigma_{\text{R}}(\mathbf{k}, 0)$ after one loop. We observe large scattering rates not only at the nodal points but on top of the whole Fermi surface. Furthermore, also notice that the maximal values appear in axial directions. Note that the slightly enhanced scattering rates around the Fermi surface can be explained by a symmetry of the Eliashberg equation for $\text{Im}\Sigma$ which is present whenever dealing with (at least somewhat) finite ordering wave vectors. We will come back to these $3k_{\text{F}}$ lines in Chapter 6. Same parameters as above: $\beta t = 50$, $m/t = 0.01$, $\lambda/t = 0.7$, $t'/t = -0.398$, $\mu/t = -2.175$.

Since this finding does not change at higher loop orders, let us directly turn to the fully converged Eliashberg solution after 10 self-consistency loops. The absence of finite ordering wave vectors is visible in Fig. 4.5 analyzing the density and surface plots or alternatively depicted in Fig. 4.3 using cuts in various directions.

Lastly, turn to the fully converged fermion self-energy or to be more precise the scattering rate at Fermi energy. The density and surface plots in Fig. 4.6 reveal that the ridge-like structure on top of the Fermi surface from the first loop is no longer present but has been traded for a high scattering rate spanning over the whole Fermi surface. Similar to the polarization, this qualitative change also occurs going from the first to the second loop order which is not really surprising due to the coupled structure of the Eliashberg equations.

How do we now proceed, since our system developed an ordering wave vector $\mathbf{Q} = \mathbf{0}$ instead of the desired finite one? Maybe we just picked an unfavorable set of parameters despite all the considerations at the chapter's beginning? We therefore varied the temperature, the mass, the coupling constant, the chemical potential and also the next nearest neighbor hopping amplitude. We changed one of these parameters at a time while keeping the others fixed as well as changed multiple parameters at the same time,

but unfortunately could not manage to obtain an ordering wave vector $\mathbf{Q} \neq \mathbf{0}$. Fig. 4.7 serves as an example of these parameter variations. To conclude, in every variation we observed this characteristic high plateau in the static polarization in the first loop, which apparently tends to smear out at higher loop orders giving rise to $\mathbf{Q} = \mathbf{0}$.

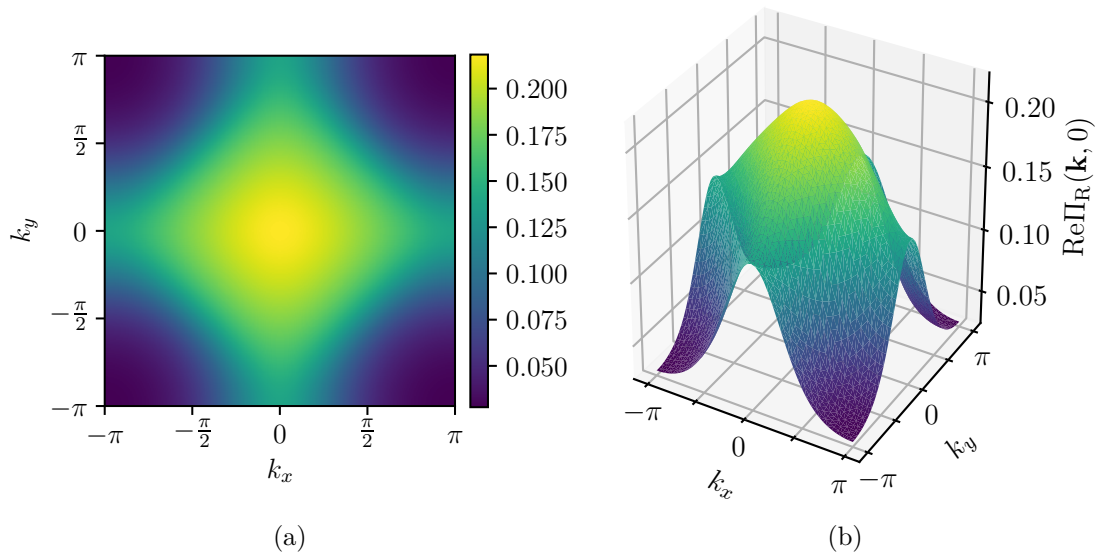


Figure 4.5.: Density (a) and surface (b) plot of the fully converged static polarization $\text{Re}\Pi_{\text{R}}(\mathbf{k}, 0)$ after 10 self-consistency loops. Note that the four small peaks at finite wave vectors encountered in the first loop are no longer present and we only observe a single large peak at $\mathbf{k} = \mathbf{0}$ now. Same parameters as above: $\beta t = 50$, $m/t = 0.01$, $\lambda/t = 0.7$, $t'/t = -0.398$, $\mu/t = -2.175$.

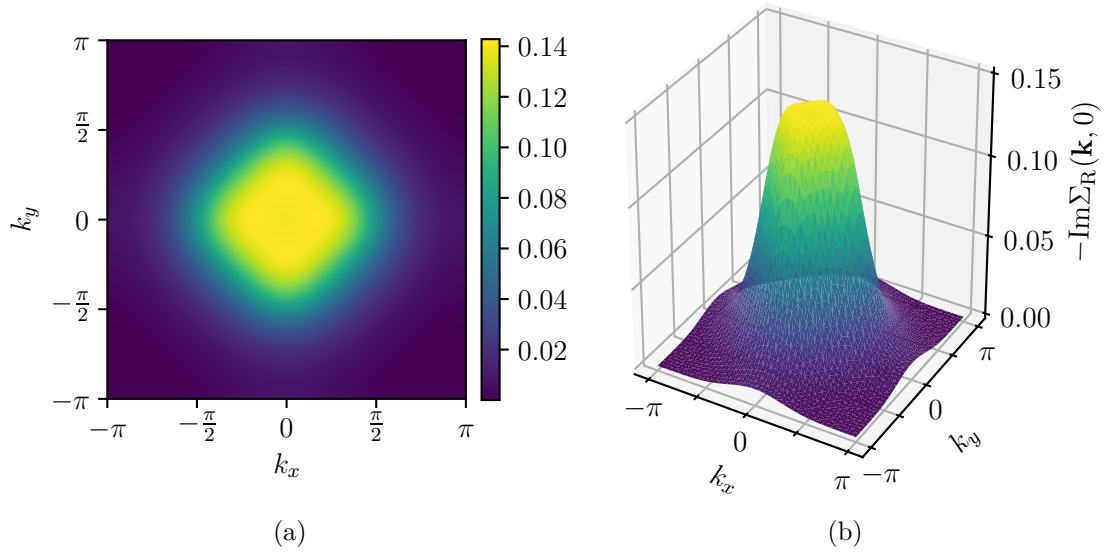


Figure 4.6.: Density (a) and surface (b) plot of the fully converged scattering rate $-\text{Im}\Sigma_{\text{R}}(\mathbf{k}, 0)$ after 10 self-consistency loops. We observe no longer scattering rate ridges but a plateau spanning over the whole Fermi surface. Same parameters as above: $\beta t = 50$, $m/t = 0.01$, $\lambda/t = 0.7$, $t'/t = -0.398$, $\mu/t = -2.175$.

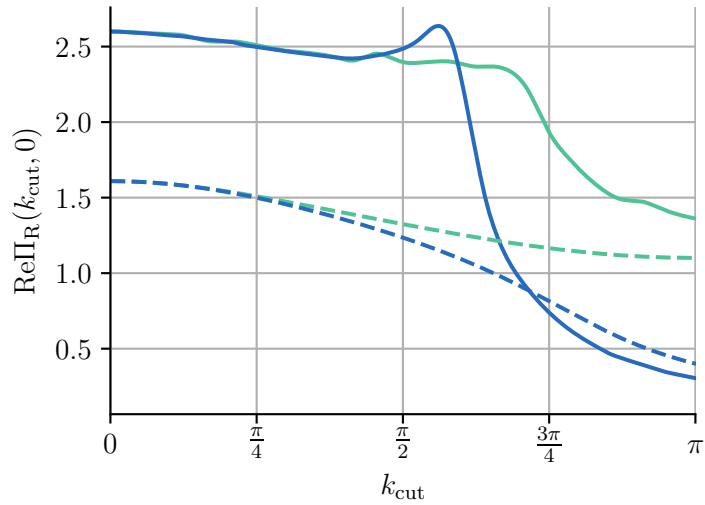


Figure 4.7.: Depicted are again various cuts of the static polarization $\text{Re}\Pi_{\text{R}}(\cdot, 0)$ in momentum space but now for a different choice of parameters which are $\beta t = 100$, $m/t = 0.001$, $\lambda/t = 2.0$, $t'/t = -0.398$ and $\mu/t = -2.175$. The blue lines correspond to a diagonal direction and we use $k_{\text{cut}} := \sqrt{k_x^2 + k_y^2}$. Moreover, the green lines display the polarization along one of the axes and we use $k_{\text{cut}} := k_x$ and set $k_y = 0$ (or vice versa). Note that the solid lines show the results after one loop and the dashed lines depict the fully converged polarization after 10 loops. Notice that the local maximum at finite wave vector from the first loop is no longer present at higher loop numbers.

5. Concavo-Convex Geometries

Since the numerical investigations presented in Chapter 4 turned out different than expected, we decided to numerically analyze a slightly altered model. This will be done in the subsequent Chapter 6. To be more specific, the plan is to trade the tight binding dispersion relation for a Fermi sheet-like one. However, as already mentioned in Section 2.2, this new dispersion relation gives rise to a qualitative different Fermi patch geometry which is depicted in Fig. 2.4. Therefore we need to review and possibly modify the analytical calculations from Chapter 3 which is the purpose of this chapter.

5.1. Scattering Rate

Fortunately, the classical scattering rate can be estimated in the same way as for the biconvex geometry and will therefore only be stated here:

$$\gamma_+^{(\text{cl})} = \frac{\lambda^2}{4v_{\text{F},-}\sqrt{A_+}} \frac{T}{\sqrt{m(T)}} \quad (5.1)$$

Note that in this new geometry a lot of constants and quantities are now hot spot dependent which is indicated by the corresponding $+/-$ subscripts. Again the expression for the classical scattering rate depends on the mass which we are going to investigate in the next section.

5.2. Renormalized Mass

The explicit form of the mass is already altered in the new geometry, since now Eq. (3.15) does not hold anymore and we have to start from Eq. (3.14) containing two integrands. However, being only interested in the functional dependence on the temperature makes our life a lot easier. Let us start from the aforementioned Eq. (3.14) with zero external

frequency and momentum

$$\begin{aligned} \text{Re } \Pi_{+,R}(\mathbf{0}, 0) = 2\lambda^2 \int_{\mathbf{q}} \int_{-\infty}^{\infty} \frac{dz}{\pi} n_F(z) & \left(\text{Re } G_{+,R}(\mathbf{q}, z) \text{Im } G_{-,R}(\mathbf{q}, z) \right. \\ & \left. + \text{Re } G_{-,R}(\mathbf{q}, z) \text{Im } G_{+,R}(\mathbf{q}, z) \right). \end{aligned} \quad (5.2)$$

Again, we will use a Sommerfeld expansion which can be justified a posteriori and arrive at

$$\begin{aligned} \text{Re } \Pi_{+,R}(\mathbf{0}, 0) = 2\lambda^2 \int_{\mathbf{q}} \int_{-\infty}^0 \frac{dz}{\pi} & \left(\text{Re } G_{+,R}(\mathbf{q}, z) \text{Im } G_{-,R}(\mathbf{q}, z) \right. \\ & \left. + \text{Re } G_{-,R}(\mathbf{q}, z) \text{Im } G_{+,R}(\mathbf{q}, z) \right). \end{aligned} \quad (5.3)$$

One expects the dominant contribution to be given by

$$\begin{aligned} \text{Re } \Pi_{+,R}(\mathbf{0}, 0) = 2\lambda^2 \int_{\mathbf{q}} \int_{-\infty}^0 \frac{dz}{\pi} & \left(\frac{z - \xi_{+,q}}{(z - \xi_{+,q})^2 + \gamma_+^2} \cdot \frac{-\gamma_-}{(z - \xi_{-,q})^2 + \gamma_-^2} \right. \\ & \left. + \frac{z - \xi_{-,q}}{(z - \xi_{-,q})^2 + \gamma_-^2} \cdot \frac{-\gamma_+}{(z - \xi_{+,q})^2 + \gamma_+^2} \right). \end{aligned} \quad (5.4)$$

Since we expect $\gamma_{\pm}(T) \sim T^p$ (with some exponent $p \in (0, \infty)$), we know that a temperature-independent $\alpha > 0$ exists (which might however depend on the Fermi velocities or the curvatures) relating the scattering rates at the two hot spots by $\gamma_-(T) = \alpha \cdot \gamma_+(T)$. Plugging this relation into the equation above we find

$$\begin{aligned} \text{Re } \Pi_{+,R}(\mathbf{0}, 0) = 2\lambda^2 \int_{\mathbf{q}} \int_{-\infty}^0 \frac{dz}{\pi} & \left(\frac{z - \xi_{+,q}}{(z - \xi_{+,q})^2 + \gamma_+^2} \cdot \frac{-\alpha\gamma_+}{(z - \xi_{-,q})^2 + \alpha^2\gamma_+^2} \right. \\ & \left. + \frac{z - \xi_{-,q}}{(z - \xi_{-,q})^2 + \alpha^2\gamma_+^2} \cdot \frac{-\gamma_+}{(z - \xi_{+,q})^2 + \gamma_+^2} \right). \end{aligned} \quad (5.5)$$

Now we are ready to apply the substitutions $z \rightarrow z\gamma_+$, $q_x \rightarrow q_x\gamma_+$ and $q_y \rightarrow q_y\sqrt{\gamma_+}$ resulting in $\text{Re } \Pi_{+,R}(\mathbf{0}, 0) \sim \sqrt{\gamma_+(T)}$ and therefore of course

$$\boxed{m(T) \sim \sqrt{\gamma_+(T)}} \quad (5.6)$$

As in Section 3.2 we reached the point where we should ask ourselves how the quantum part of the scattering rate scales with temperature. Is the classical part in the concavo-convex geometry again subleading compared to the quantum one? To put it differently, may we again proceed by $m(T) \sim \sqrt{\gamma_+^{(\text{qu})}(T)}$ and what is the precise value of the corresponding critical exponent? Since it turns out that the imaginary part of the polarization helps us to answer this question, we will first derive it and come back to the

discussion of classical vs. quantum part of the scattering rate at the end of this chapter, hence Section 5.4.

5.3. Imaginary Part of Polarization

Let us now turn to the imaginary part of the polarization. Again, one of our goals is to investigate possible Fermi surface changes via the dynamical critical exponents. As in Section 3.4, the hot spot version of Eq. (2.13) will serve as a starting point. Note that this formula is still valid for the concavo-convex geometry, since no point group symmetries had been exploited in the derivation, hence

$$\begin{aligned} \text{Im } \Pi_{+,R}(\mathbf{k}, \Omega) &= 2\lambda^2 \int_{\mathbf{q}} \int_{-\infty}^{\infty} \frac{dz}{\pi} (n_F(z) - n_F(z + \Omega)) \\ &\quad \cdot \text{Im } G_{+,R}(\mathbf{k} + \mathbf{q}, \Omega + z) \text{Im } G_{-,R}(\mathbf{q}, z). \end{aligned} \quad (5.7)$$

In complete analogy to the biconvex calculation of Section 3.4 we approximate

$$\text{Im } \Pi_{+,R}(\mathbf{k}, \Omega) = 2\lambda^2 \Omega \int_{\mathbf{q}} \frac{\gamma_+}{(\xi_{+, \mathbf{k} + \mathbf{q}})^2 + \gamma_+^2} \cdot \delta(\xi_{-, \mathbf{q}}) \quad (5.8)$$

where we used the aforementioned expansion of the second Fermi distribution in Ω and approximated one Lorentzian by a delta distribution. The integration in q_x -direction gives

$$\begin{aligned} \text{Im } \Pi_{+,R}(\mathbf{k}, \Omega) &= \frac{\lambda^2 \Omega}{2\pi^2 v_{F,-} \gamma_+} \int_{-\infty}^{\infty} dq_y \\ &\quad \frac{1}{\left(\frac{|a|}{2\gamma_+ v_{F,-}} \cdot q_y^2 - \frac{\text{sgn}(a)\kappa_+ k_y}{\gamma_+} \cdot q_y + \frac{\text{sgn}(a)\xi_{+, \mathbf{k}}}{\gamma_+} \right)^2 + 1} \end{aligned} \quad (5.9)$$

where we already organized the denominator in powers of q_y and introduced the abbreviation $a := v_{F,+}\kappa_- - v_{F,-}\kappa_+$. For the case of aligning Fermi surfaces ($a = 0$) we proceed with the substitution $x := \frac{\kappa_+ |k_y|}{\gamma_+} \cdot q_y - \frac{\xi_{+, \mathbf{k}} \text{sgn}(k_y)}{\gamma_+}$ (in the case $k_y \neq 0$) and apply for example the residue theorem to solve the remaining integral $\int dx (x^2 + 1)^{-1} = \pi$. We therefore have already found the expression for the polarization's imaginary part in the case $a = 0$ which reads

$$\boxed{\text{Im } \Pi_{+,R}(\mathbf{k}, \Omega, a = 0) = \frac{\lambda^2}{2\pi v_{F,-} \kappa_+} \cdot \frac{\Omega}{|k_y|}} \quad (5.10)$$

Interestingly we arrive at a temperature-independent result in this special case $a = 0$. We will come back to this Landau damping term (in k_y -direction) in the following Section

5.4.

Let us now turn to the case of non-aligning Fermi surfaces ($a \neq 0$). Also here the integral (5.9) may be solved by applying the residue theorem. Since the computation itself is not really enlightening and slightly longer, it is only provided in Appendix A.5. However more exciting is the result which reads

$$\text{Im } \Pi_{+,R}(\mathbf{k}, \Omega, a \neq 0) = \frac{\lambda^2 \Omega}{2\pi \sqrt{v_{F,-}|a|}} \cdot \frac{\sqrt{\sqrt{\eta_{\mathbf{k}}^2 + \gamma_+^2} - \eta_{\mathbf{k}}}}{\sqrt{\eta_{\mathbf{k}}^2 + \gamma_+^2}} \quad (5.11)$$

where we defined $\eta_{\mathbf{k}} := \text{sgn}(a) \left(\xi_{+,\mathbf{k}} - \frac{\kappa_+^2 v_{F,-}}{2a} k_y^2 \right)$ which might be viewed as the equivalent to $e_{\mathbf{k}}$ used in the biconvex geometry. One may ask how the results of the two cases $a = 0$ and $a \neq 0$ are related. An explicit calculation shows

$$\lim_{a \rightarrow 0} \text{Im } \Pi_{+,R}(\mathbf{k}, \Omega, a \neq 0) = 2 \cdot \text{Im } \Pi_{+,R}(\mathbf{k}, \Omega, a = 0) . \quad (5.12)$$

This discontinuity at $a = 0$ makes sense, since for $a \neq 0$ the integrand displayed four poles while for $a = 0$ only two were present. We therefore could have already guessed to be off by a factor of 2 when taking the limit $a \rightarrow 0$.

Let us now turn to the limits we previously looked at in the biconvex geometry. First, consider the zero temperature limit ($\gamma_+ \rightarrow 0$)

$$\text{Im } \Pi_{+,R}(\mathbf{k}, \Omega, a \neq 0, T = 0) = \frac{\lambda^2}{\pi \sqrt{2v_{F,-}|a|}} \cdot \frac{\Omega \cdot \theta(-\eta_{\mathbf{k}})}{\sqrt{|\eta_{\mathbf{k}}|}} \quad (5.13)$$

which leads to exactly the same dynamical critical exponents as for the biconvex geometry, namely $z_{\perp} = 5/2$ and $z_{\parallel} = 3$. Therefore, we expect also here the renormalized Fermi surface close to the hot spots to be of the form $k_x \sim |k_y|^{12/5}$ meaning we again find dynamical nesting.

Lastly, consider the case of vanishing external momenta

$$\text{Im } \Pi_{+,R}(\mathbf{0}, \Omega, a \neq 0) = \frac{\lambda^2}{2\pi \sqrt{v_{F,-}|a|}} \cdot \frac{\Omega}{\sqrt{\gamma_+}} . \quad (5.14)$$

Again we observe that the term $\sim \frac{\Omega}{\sqrt{|\eta_{\mathbf{k}}|}}$ in Eq. (5.13) transforms into a quite similar looking term $\sim \frac{\Omega}{\sqrt{\gamma_+}}$ when turning from the zero temperature limit to the regime of finite temperature but zero external momenta.

5.4. Scattering Rate Revisited

In contrast to the biconvex Fermi patch geometry we are not aware of any RPA treatments for this modified concavo-convex geometry. As already mentioned in Section 5.2 it would however be quite useful to be in possession of such RPA treatments, since one may estimate the temperature dependence of the scattering rate's quantum part by using the zero temperature RPA result in combination with ω/T -scaling. We will therefore try to compute the fermionic self-energy in a RPA fashion in this section.

Let us start by calculating the bare fermionic bubble for the special case $\xi_{+,q} = -\xi_{-,q}$. For simplicity we set the Fermi velocities $v_{F,+} = v_{F,-} = 1$ and curvatures $\kappa_+ = \kappa_- = 2$, hence we work with

$$\xi_{+,q} = q_x - q_y^2, \quad (5.15)$$

$$\xi_{-,q} = -q_x + q_y^2. \quad (5.16)$$

At $T = 0$ the RPA polarization is given by

$$\Pi_+^{(\text{RPA})}(k) = -2\lambda^2 \int \frac{d^3q}{(2\pi)^3} G_{-,0}(q) G_{+,0}(k+q) \quad (5.17)$$

$$= -2\lambda^2 \int \frac{d^3q}{(2\pi)^3} \frac{1}{iq_0 - \xi_{-,q}} \frac{1}{i(k_0 + q_0) - \xi_{+,k+q}}. \quad (5.18)$$

The substitutions $q_0 \rightarrow q_0 - k_0/2$ and $q_x \rightarrow -q_x + q_y^2$ give rise to

$$\Pi_+^{(\text{RPA})}(k) = 2\lambda^2 \int \frac{d^3q}{(2\pi)^3} \frac{1}{q_x - i(q_0 - \frac{k_0}{2})} \frac{1}{q_x + i(q_0 + \frac{k_0}{2}) + \xi_{-,k} + 2k_y q_y}. \quad (5.19)$$

Applying the residue theorem with respect to the q_x -integral yields

$$\Pi_+^{(\text{RPA})}(k) = \frac{i\lambda^2}{2\pi^2} \left(\int_{\frac{|k_0|}{2}}^{\infty} dq_0 - \int_{-\infty}^{-\frac{|k_0|}{2}} dq_0 \right) \int_{-\infty}^{\infty} dq_y \frac{1}{2k_y q_y + \xi_{-,k} + 2iq_0}. \quad (5.20)$$

Note that for $k_y = 0$ the q_y -integral diverges, hence consider only the case $k_y \neq 0$. Let us proceed with the substitution $q_y \rightarrow q_y - \xi_{-,k}$ resulting in

$$\Pi_+^{(\text{RPA})}(k) = \frac{i\lambda^2}{2\pi^2} \left(\int_{\frac{|k_0|}{2}}^{\infty} dq_0 - \int_{-\infty}^{-\frac{|k_0|}{2}} dq_0 \right) \frac{1}{2k_y} \int_{-\infty}^{\infty} dq_y \frac{1}{q_y + i\frac{q_0}{k_y}} \quad (5.21)$$

$$= \frac{\lambda^2}{4\pi|k_y|} \left(\int_{\frac{|k_0|}{2}}^{\infty} dq_0 + \int_{-\infty}^{-\frac{|k_0|}{2}} dq_0 \right) \quad (5.22)$$

where the q_y -integral could be either solved directly by using the antiderivative, hence the complex logarithm, or by splitting the integrand first into real and imaginary part,

observing that the principle value of the real part vanishes and applying the residue theorem for the imaginary part. Since the discovered expression diverges, we proceed with the renormalized polarization

$$\delta\Pi_+^{(\text{RPA})}(k) := \Pi_+^{(\text{RPA})}(k) - \Pi_+^{(\text{RPA})}(0) \quad (5.23)$$

$$= \frac{\lambda^2}{4\pi} \left(\lim_{x \rightarrow \infty} x - \left| \frac{k_0}{k_y} \right| \right) - \frac{\lambda^2}{4\pi} \lim_{x \rightarrow \infty} x \quad (5.24)$$

and therefore arrive for $v_{F,+} = v_{F,-} = 1$ and $\kappa_+ = \kappa_- = 2$ at the final expression for the RPA polarization

$$\boxed{\delta\Pi_+^{(\text{RPA})}(k) = -\frac{\lambda^2}{4\pi} \left| \frac{k_0}{k_y} \right|} \quad (5.25)$$

which turns out to be a Landau damping term in k_y -direction. Let us compare this result to Eliashberg theory by performing the analytic continuation $k_0 \rightarrow i\Omega + 0^+$ to real frequencies which gives

$$\delta\Pi_{+,R}^{(\text{RPA})}(\mathbf{k}, \Omega) = \frac{i\lambda^2}{4\pi} \frac{\Omega}{|k_y|}. \quad (5.26)$$

Interestingly this is exactly the result we got from the finite temperature Eliashberg calculation for $v_{F,+} = v_{F,-} = 1$ and $\kappa_+ = \kappa_- = 2$ in the previous section (Eq. (5.10)).

The derived RPA result (5.25) reminds us also of the RPA polarization $\sim \left| \frac{k_0}{k_y} \right|$ for Ising-nematic ordering in the corresponding hot spot treatment [2]. This resemblance is also the reason the following calculation of the fermionic self-energy will be extremely similar to the corresponding calculation for Ising-nematic ordering. We will therefore follow along the lines of Sachdev [2]. Let us start with

$$\Sigma_+^{(\text{RPA})}(k) = \lambda^2 \int \frac{d^3q}{(2\pi)^3} G_{-,0}(k-q) D_+^{(\text{RPA})}(q) \quad (5.27)$$

$$= \lambda^2 \int \frac{d^3q}{(2\pi)^3} \frac{1}{i(k_0 - q_0) - \xi_{-,k-q} q_y^2 - \delta\Pi_+^{(\text{RPA})}(q)}. \quad (5.28)$$

Note that the we dropped the irrelevant terms q_0^2 and q_x^2 in the boson propagator. Being only interested in the frequency-dependence right at the hot spot, we proceed with

$$\Sigma_+^{(\text{RPA})}(\mathbf{k} = \mathbf{0}, k_0) = -\lambda^2 \int \frac{d^3q}{(2\pi)^3} \frac{1}{q_x - i(k_0 - q_0) - q_y^2} \frac{1}{q_y^2 + \frac{\lambda^2}{4\pi} \left| \frac{q_0}{q_y} \right|}. \quad (5.29)$$

Carefully evaluating the q_x -integral and afterwards computing the q_0 -integral yields

$$\Sigma_+^{(\text{RPA})}(\mathbf{0}, k_0) = -\frac{i\lambda^2 \text{sgn}(k_0)}{4\pi^2} \int_{-\infty}^{\infty} dq_y \int_0^{|k_0|} dq_0 \frac{|q_y|}{|q_y|^3 + \frac{\lambda^2}{4\pi} q_0} \quad (5.30)$$

$$= -\frac{2i \text{sgn}(k_0)}{\pi} \int_0^{\infty} dq_y q_y \ln \left(\frac{q_y^3 + \frac{\lambda^2}{4\pi} |k_0|}{q_y^3} \right). \quad (5.31)$$

The final substitution $q_y \rightarrow q_y \sqrt[3]{\frac{\lambda^2}{4\pi} |k_0|}$ already provides the desired scaling of $\text{sgn}(k_0) |k_0|^{2/3}$ and with all prefactors we end up with

$$\Sigma_+^{(\text{RPA})}(\mathbf{0}, k_0) = -\frac{2i\lambda^{4/3}}{\sqrt{3}(4\pi)^{2/3}} \cdot \text{sgn}(k_0) \cdot |k_0|^{2/3} \quad (5.32)$$

Exploiting ω/T -scaling, we may again estimate the temperature-dependence of the scattering rate's quantum part as

$$\gamma_+^{(\text{qu})}(T) \sim T^{2/3} \quad (5.33)$$

Since we found exactly the same temperature-dependence as in Section 3.2, we can apply the same line of reasoning here. Hence, we also expect the classical scattering rate to be subleading compared to the quantum part. Due to Eq. (5.6) we again expect the mass to scale as $m(T) \sim T^{1/3}$. Note that, since $\frac{2}{3} \in (0, 1]$, the Sommerfeld expansion can again be a posteriori justified (see Eq. (3.38)). Furthermore, Eq. (5.1) unveils again the (subleading) classical scattering rate's temperature dependence $\gamma_+^{(\text{cl})}(T) \sim T^{5/6}$.

Note that the above presented results were only derived for a Fermi patch geometry with Fermi velocities $v_{F,+} = v_{F,-} = 1$ and curvatures $\kappa_+ = \kappa_- = 2$. Unfortunately, we had no time left to generalize these RPA calculations to Fermi surface geometries with arbitrary Fermi velocities and curvatures.

However, the subsequent scaling argument following [2] provides hope that $\gamma_+^{(\text{qu})}(T) \sim T^{2/3}$ may also hold in the general case. Let us start by considering the free fermionic part of the hot spot action (2.6). This term suggests the following rescalings after having performed a ‘‘decimation’’ step in a momentum shell RG program like $k'_x = b^2 k_x$ and $k'_y = b k_y$. How do we rescale the frequency now? The zero temperature limit of the polarization's imaginary part in Eliashberg theory (Eq. (5.13)) yields

$$\frac{|k'_0| \cdot \theta(-\eta_{\mathbf{k}'})}{\sqrt{|\eta_{\mathbf{k}'}|}} = b^{z-1} \cdot \frac{|k_0| \cdot \theta(-\eta_{\mathbf{k}})}{\sqrt{|\eta_{\mathbf{k}}|}} \quad (5.34)$$

where we rescaled the frequency as $k'_0 = b^z k_0$. Matching scaling dimensions with the

k_y^2 -term appearing in the Ornstein-Zernike form (2.5) gives $z = 3$. Moreover, we have to rescale the (momentum-dependent) fields like $\psi' = b^{-4}\psi$ and $\phi' = b^{-4}\phi$ which give rise to a marginal coupling constant $\lambda' = \lambda$. Let us assume $\text{Im } \Sigma_+(\mathbf{0}, k_0) \sim k_0^p$ with a so far undetermined exponent $p \in \mathbb{R}$. Now we match scaling dimensions with the purely fermionic part of the action and find $p = 2/3$, due to the marginal coupling. Hence, we ultimately obtain

$$\text{Im } \Sigma_+(\mathbf{0}, k_0) \sim k_0^{2/3} \tag{5.35}$$

also in the general case of arbitrary Fermi velocities $v_{F,+}, v_{F,-} > 0$ and curvatures $\kappa_+, \kappa_- > 0$. This result again indicates clear non-Fermi liquid behavior.

6. Fermi Sheet Model

After having revisited the analytical calculations in the last chapter, let us now turn to the corresponding numerical investigations. As in Chapter 4 we will study the full theory (2.1) but now use a Fermi sheet-like dispersion relation which is nothing else than the standard tight binding dispersion relation with direction-dependent nearest neighbor hopping amplitudes t_x and t_y . We will therefore be using

$$\xi_{\mathbf{k}} = -t_x \cos(k_x) - t_y \cos(k_y) - \mu \quad (6.1)$$

throughout this chapter.

6.1. Numerical Setup

Due to the great similarity of code used here and the one used for the calculation presented in Chapter 4, we will only state the differences here. First, note that the Fermi sheet dispersion relation only has D_2 instead of D_4 symmetry anymore, we therefore need to solve the Eliashberg equation on a quadrant instead of an octant now. Secondly, setting $t_x = 1$ we are still left to choose λ , β , m , t_y and μ . We set the coupling constant $\lambda/t_x = 1.0$, choose an inverse temperature $\beta t_x = 50$ and fix the renormalized mass $m/t_x = 0.01$. Furthermore, we set $t_y/t_x = 0.3$ such that the ratio is on the one hand not too close to zero (since this would basically reduce the problem to one dimension), but on the other hand is also not too close to one, hence we still deal with a significantly direction-dependent hopping. How do we now choose the chemical potential? This can again be done with the help of the aforementioned $2k_F$ lines which are depicted in Fig. 6.1. We decided to set $\mu/t_x = -0.55$, since then the $2k_F$ lines are still reasonable distant along the k_x -axis. Moreover, we pin the Fermi surface to the point $\mathbf{k}_{\text{pin}} = (1.318, 0.0)$ in the following. With these parameters we obtain $2k_F$ lines intersecting in the points $\mathbf{Q}_1 := (2 \cos^{-1}(-\mu/t_x), \pi) = (1.98, \pi)$ and $-\mathbf{Q}_1$. As for example pointed out by Holder and Metzner [40] these intersections are of particular interest, since they tend to give rise to the maxima of the static polarization and therefore also the static (dressed) susceptibility. We therefore expect two ordering wave vectors roughly around $(\pm 1.98, \pi)$ being present in the following numerical investigation.

Which points on the Fermi surface are now connected by these expected ordering wave vectors? Let us for simplicity focus on the nesting vector with positive k_x -component, hence \mathbf{Q}_1 . Due to inversion symmetry it connects the two points $\pm\mathbf{Q}_1/2 = \pm(0.99, \pi/2)$ on the Fermi surface, hence we expect relatively large scattering rates in the vicinity of these points. However, notice that these might not be the only points in the Brillouin zone with increased scattering rates, since the nesting vector \mathbf{Q}_1 is also really close to connecting the points $(-\cos^{-1}(-\mu/t_x - t_y/t_x), 0) = (-1.32, 0)$ and $(\cos^{-1}(-\mu/t_x + t_y/t_x), 0) = (0.55, \pi)$, since $\mathbf{Q}_2 := (0.55, \pi) - (-1.32, 0) = (1.87, \pi)$ is close to $(1.98, \pi) = \mathbf{Q}_1$. These findings are also visualized in Fig. 6.1. However, note that of course \mathbf{Q}_2 is a nesting vector itself, since it connects two points on the Fermi surface with parallel tangents as well, but cannot be determined by the simple $2k_F$ condition $\xi_{(\mathbf{k}+\mathbf{G})/2} = 0$. It is therefore quite likely that we will observe multiple pairs of hot spots – or even high scattering rates on top of the whole Fermi surface – in the following numerical investigation.

6.2. First Results

Having chosen promising parameters in the previous section, let us now turn to the numerical solution of the Eliashberg equations (2.12) and (2.13) using the scheme described in Section 2.5. As for the tight binding numerics, we want to start off by looking at the static polarization $\text{Re } \Pi_{\mathbf{R}}(\mathbf{k}, 0)$ which is depicted in Fig. 6.2. This figure shows the results after one loop (Figs. 6.2a and 6.2b) as well as the fully converged quantities after the tenth loop (Figs. 6.2c and 6.2d). We observe that in contrast to our previous numerical investigations from Section 4, the solution does not change qualitatively with increasing loop order. In particular, the two tall peaks at finite wave vectors at the Brillouin zone’s edge turn out to be stable although their height drops from 1.784 after the first loop to 1.286 at convergence. At tenth loop order we find the corresponding ordering wave vectors $\mathbf{Q} = \pm(2.009, 3.142)$. Note that this vector is really close to the nesting vectors \mathbf{Q}_1 and \mathbf{Q}_2 from the previous section.

Let us now take a brief look at the scattering rate at Fermi energy, hence $-\text{Im } \Sigma_{\mathbf{R}}(\mathbf{k}, 0)$. The density and surface plots are depicted in Fig. 6.3a and 6.3b for the first loop and in the Figs. 6.3c and 6.3d corresponding to the fully converged solution after the tenth loop. Similar to the static polarization, the solution obtained in the first loop order remains qualitatively valid at higher loop orders. Furthermore, we observe four sheet-like regions with high scattering rates. Although one might already guess that two “inner” ridges stem from the underlying Fermi surface, it is at this point completely unclear how the two “outer” ones arise. We therefore want to stop guessing but analyze the situation

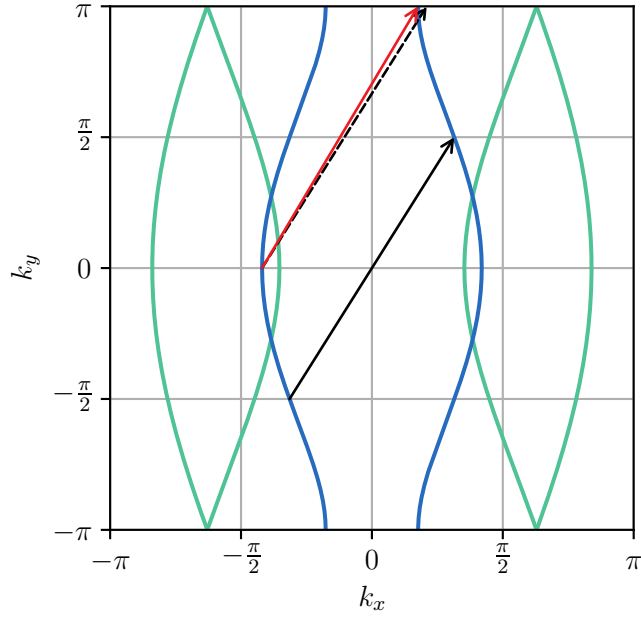


Figure 6.1.: The blue lines depict the Fermi surface arising from the Fermi sheet-like dispersion relation (6.1) for $t_y/t_x = 0.3$ and $\mu/t_x = -0.55$. Moreover, the resulting $2k_F$ lines are shown green. The solid black arrow depicts one of the two nesting vectors arising from the $2k_F$ line intersections at $(\pm 1.98, \pi)$. By construction this vector \mathbf{Q}_1 connects the two points $\pm \mathbf{Q}_1/2 = \pm(0.99, \pi/2)$ on the Fermi surface. However, note that this vector is also really close to connecting the points $(-1.32, 0)$ and $(0.55, \pi)$. To illustrate this we simply moved the nesting vector \mathbf{Q}_1 to the starting point $(-1.32, 0)$. This shifted vector is depicted by the dashed black arrow and ends in the point $(-1.32, 0) + (1.98, \pi) = (0.66, \pi)$ which is of course close to $(0.55, \pi)$. By the red arrow we depict the nesting vector $\mathbf{Q}_2 = (1.87, \pi)$ which could not be determined by the simple $2k_F$ condition $\xi_{(\mathbf{k}+\mathbf{G})/2} = 0$ but has of course also be considered.

more quantitatively by first visualizing the interacting Fermi surface. This is among other things shown in Fig. 6.4.

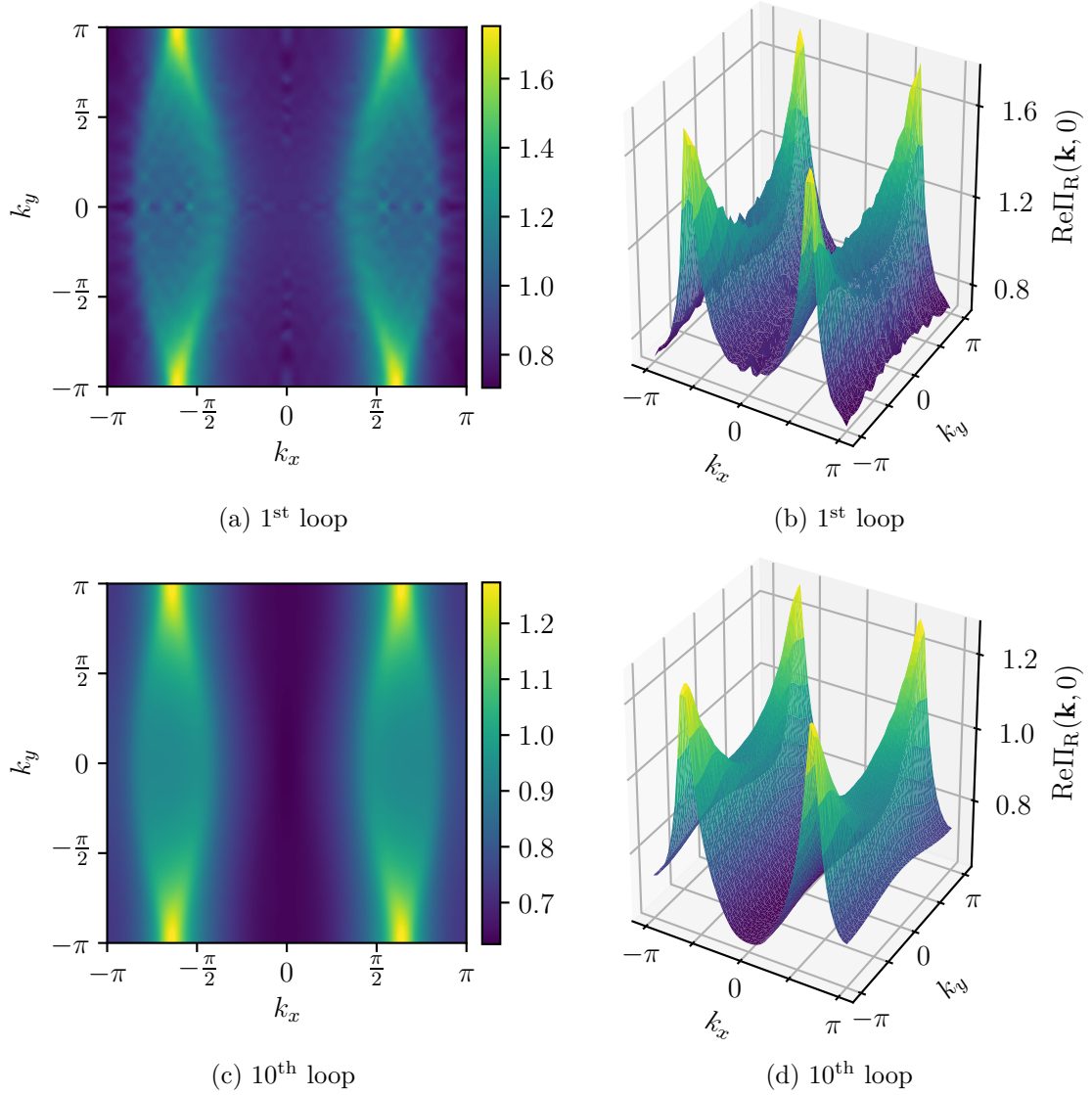


Figure 6.2.: Density and surface plots of the static polarization $\text{Re} \Pi_{\text{R}}(\mathbf{k}, 0)$. While the upper panels (a) and (b) depict the results after one loop, the lower panels (c) and (d) show the fully converged solution after the tenth loop. We observe a stable solution qualitatively already present at first loop order and even more importantly two clear peaks at finite wave vectors $\mathbf{Q} = \pm(2.009, 3.142)$. Parameters: $\beta t_x = 50$, $m/t_x = 0.01$, $\lambda/t_x = 1.0$, $t_y/t_x = 0.3$, $\mu/t_x = -0.55$.

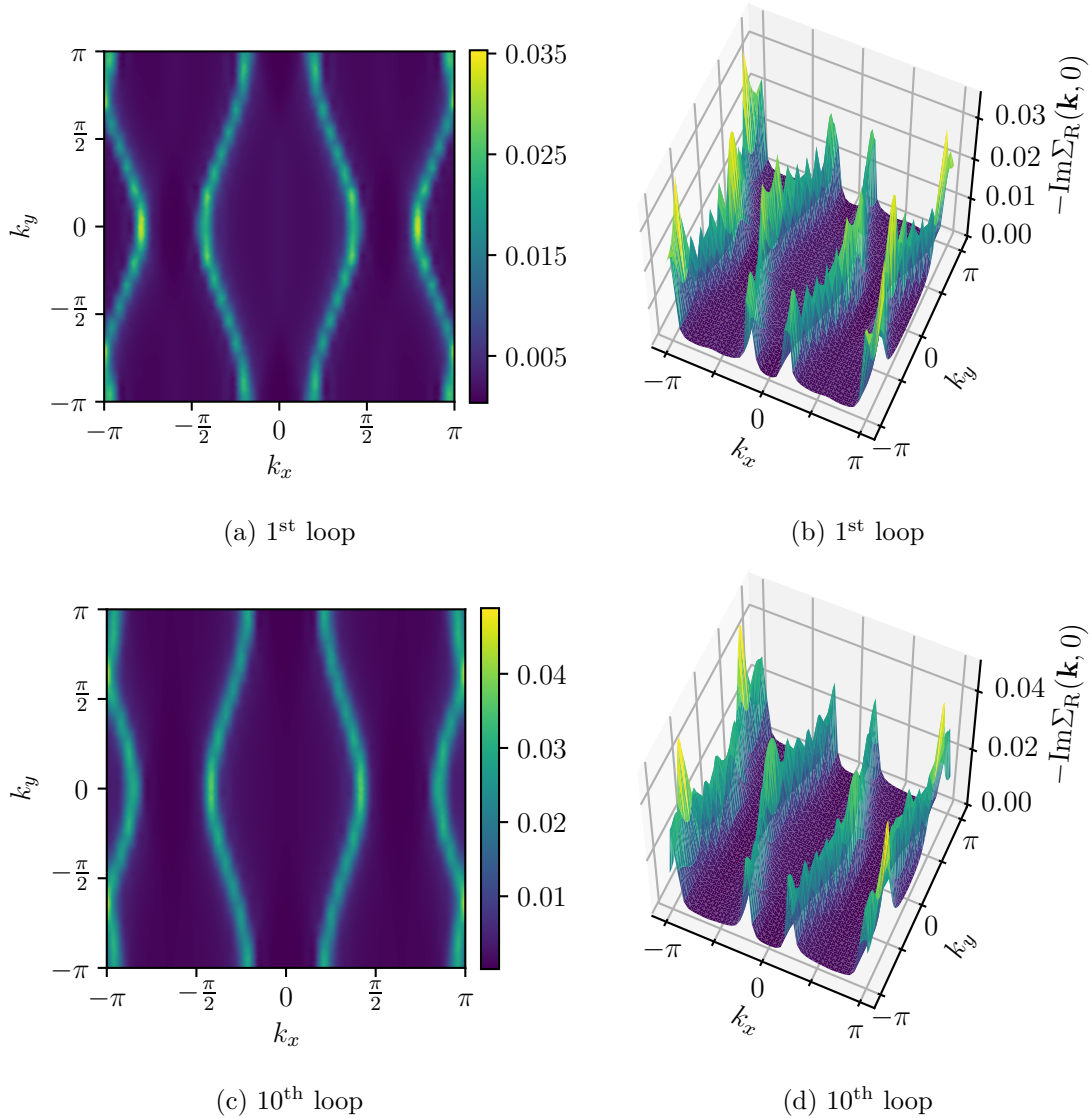


Figure 6.3.: Density and surface plots of the scattering rate at Fermi energy, hence $-\text{Im}\Sigma_R(\mathbf{k}, 0)$. While the upper panels (a) and (b) depict the results after one loop, the lower panels (c) and (d) show the fully converged solution after the tenth loop. We observe four sheet-like regions with high scattering rates. It turns out that the inner two ridges stem from the (interacting) Fermi surface while the outer two are caused by some kind of symmetry the Eliashberg equation for the fermionic self-energy shows in the presence of finite ordering wave vectors. Same parameters as above: $\beta t_x = 50$, $m/t_x = 0.01$, $\lambda/t_x = 1.0$, $t_y/t_x = 0.3$, $\mu/t_x = -0.55$.

Let us turn to the concepts used in Fig. 6.4. The first one is the interacting Fermi surface which is defined by all wave vectors \mathbf{k} fulfilling the condition

$$\xi_{\mathbf{k}}^{(\text{int})} := \xi_{\mathbf{k}} + \text{Re} \Sigma_{\text{R}}(\mathbf{k}, 0) = 0 \quad (6.2)$$

which generalizes the non-interacting condition $\xi_{\mathbf{k}} = 0$ by taking corrections from the real part of the fermionic self-energy $\text{Re} \Sigma_{\text{R}}$ to the dispersion relation into account. The contour lines arising from this condition are depicted by dashed black lines in Fig. 6.4. We observe that they nicely match two of the already encountered scattering rate ridges and therefore it seems natural to regard the (interacting) Fermi surface as the reason for their presence [20].

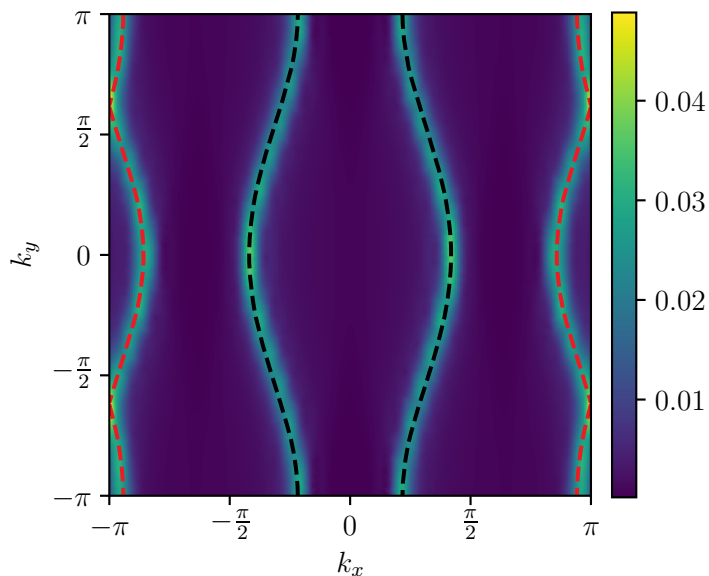


Figure 6.4.: Density plot of the fully converged static polarization $\text{Re} \Pi_{\text{R}}(\mathbf{k}, 0)$ at tenth self-consistency loop order. Furthermore, we show the interacting Fermi surface (defined by the condition (6.2)) by the two dashed black lines. Moreover, we also depict the two $3k_{\text{F}}$ lines defined by the condition (6.10) as dashed red lines. Same parameters as above: $\beta t_x = 50$, $m/t_x = 0.01$, $\lambda/t_x = 1.0$, $t_y/t_x = 0.3$, $\mu/t_x = -0.55$.

But what is the origin of the two other sheet-like structures of the scattering rate we observe in the Figs. 6.3 and 6.4? At first appearance one might think that these ridges are caused by large coupling constants which can result in strong Fermi surface changes. This would be due to strong corrections of the non-interacting dispersion relation $\xi_{\mathbf{k}}$ by large values $\text{Re} \Sigma_{\text{R}}(\mathbf{k}, 0)$. Since we just checked that this possibility in Fig. 6.4, this is of course not an option anymore. Instead, it turns out that the two unexplained scattering rate ridges stem from some kind of symmetry that the Eliashberg equation for the fermionic self-energy (2.10) contains in the presence of finite ordering wave vectors

$\mathbf{Q} = 2k_F$. Let us therefore first recapitulate the equation

$$\Sigma(k) = \frac{\lambda^2}{\beta V} \sum_q G(k - q)D(q). \quad (6.3)$$

Similar to Section 3.1, we set the external momentum onto the Fermi surface, the external frequency to zero and take only classical fluctuations into account, yielding

$$\Sigma^{(\text{cl})}(\mathbf{k}_F, 0) = \frac{\lambda^2}{\beta V} \sum_q G(\mathbf{k}_F - \mathbf{q}, 0)D(\mathbf{q}, 0) \quad (6.4)$$

$$= \frac{\lambda^2}{\beta V} \sum_{q \approx Q} G(\mathbf{k}_F - \mathbf{q}, 0)D(\mathbf{q}, 0) \quad (6.5)$$

where in the second step we exploited that the main contribution should come from momenta \mathbf{q} in the vicinity of $\pm \mathbf{Q} = 2k_F$. In a similar fashion we argue for an external momentum of $\mathbf{k}_F + \mathbf{Q}$:

$$\Sigma^{(\text{cl})}(\mathbf{k}_F + \mathbf{Q}, 0) = \frac{\lambda^2}{\beta V} \sum_q G(\mathbf{k}_F + \mathbf{Q} - \mathbf{q}, 0)D(\mathbf{q}, 0) \quad (6.6)$$

$$= \frac{\lambda^2}{\beta V} \sum_{q \approx Q} G(\mathbf{k}_F + \mathbf{Q} - \mathbf{q}, 0)D(\mathbf{q}, 0) \quad (6.7)$$

$$\approx \frac{\lambda^2}{\beta V} \sum_{q \approx Q} G(\mathbf{k}_F - \mathbf{q}, 0)D(\mathbf{q}, 0) \quad (6.8)$$

$$= \Sigma^{(\text{cl})}(\mathbf{k}_F, 0). \quad (6.9)$$

Since $\mathbf{k}_F + \mathbf{Q} \approx 3k_F$, we will refer to these lines as $3k_F$ lines. Can we also interpret these $3k_F$ lines from a more physical point of view? As depicted in Fig. 6.5 it turns out that we can, since we may view $3k_F$ lines as a product of a decay “channel” present for finite ordering wave vectors $\mathbf{Q} = 2k_F$.

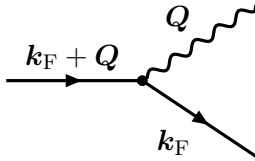


Figure 6.5.: Decay of fermion (straight line) carrying momentum $\mathbf{k}_F + \mathbf{Q}$, hence located on a $3k_F$ line, into a fermion living on the Fermi surface and a boson (wiggly line) carrying the nesting vector $\mathbf{Q} = 2k_F$. Note that this process is quite likely to take place, since the susceptibility is peaked at $\pm \mathbf{Q}$.

Let us not forget that we still have to validate these $3k_F$ lines on the numerical side. In Fig. 6.4 we therefore simply shifted the (interacting) Fermi surface by the numerically determined ordering wave vectors. This amounts to solving the (interacting) $3k_F$ line

condition

$$\xi_{(\mathbf{k}+\mathbf{G})/3}^{(\text{int})} = 0 \quad (6.10)$$

for any reciprocal lattice vector \mathbf{G} . Since we observe an almost perfect agreement of the $3k_F$ lines with the (numerically encountered) additional ridges of the scattering rate, we consider this case to be solved.

6.3. Dynamical Properties

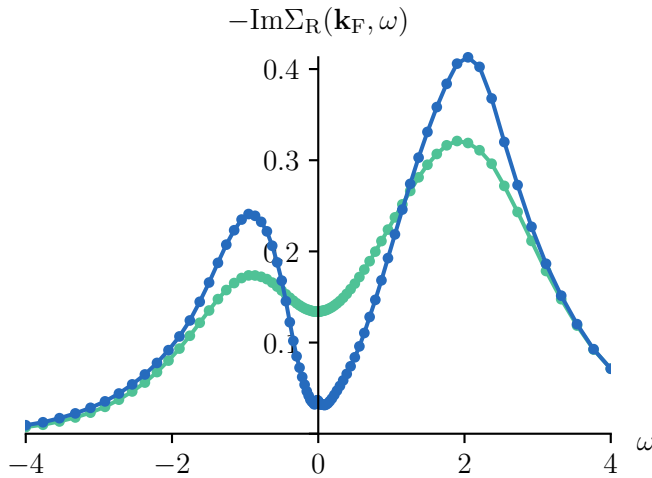


Figure 6.6.: We show the fully converged imaginary part of the fermionic self-energy $-\text{Im}\Sigma_{\text{R}}(\mathbf{k}_{\text{F}}, \omega)$ as a function of the frequency ω and set the momentum to $\mathbf{k}_{\text{F}} = (1.318, 0.0)$, hence on the Fermi surface. Note that for both curves we used the parameters $\lambda/t_x = 1.0$, $t_y/t_x = 0.3$ and $\mu/t_x = -0.55$. Moreover, the blue line arises for an inverse temperature $\beta t_x = 50$ and a fixed mass $m/t_x = 0.01$. However, the green line stems from a numerical calculation at inverse temperature $\beta t_x = 5$ and a self-consistently determined gap. We will use this data set in advance and come back to its origin in the following section.

Having only considered static quantities so far, let us also take a look at the frequency-dependence of both the fermionic and bosonic self-energies. Let us begin with the former. Fig. 6.6 shows the imaginary part of the self-energy $-\text{Im}\Sigma_{\text{R}}(\mathbf{k}_{\text{F}}, \omega)$ as function of the frequency ω and for a fixed wave vector $\mathbf{k}_{\text{F}} = (1.318, 0.0)$ lying on the Fermi surface. For both temperatures $\beta t_x = 50$ and $\beta t_x = 5$ we observe that the zero temperature power-law behavior at small frequencies ω is no longer present due to the finite scattering rate at $T > 0$. Moreover, one might also guess the $\omega^{2/3}$ scaling at intermediate frequencies. However, notice that the two intersections with the y -axis provide a more rigorous way to check the expected $T^{2/3}$ -scaling discussed in Section 5.4. Therefore, we compute the

ratio of y-axis intersections $\gamma(\beta = 5)/\gamma(\beta = 50) = 3.81$ and compare it to the term $(50/5)^{2/3} = 4.64$, meaning we find at least qualitative agreement.

Let us also have a quick look at the imaginary part of the boson's self-energy which is depicted in Fig. 6.7. As above, we keep the momentum fixed and set it in this case to the numerically determined ordering wave vector $\mathbf{Q} = (2.009, 3.141)$. As already expected by Eq. (5.14) we observe a linear regime for small frequencies ω .

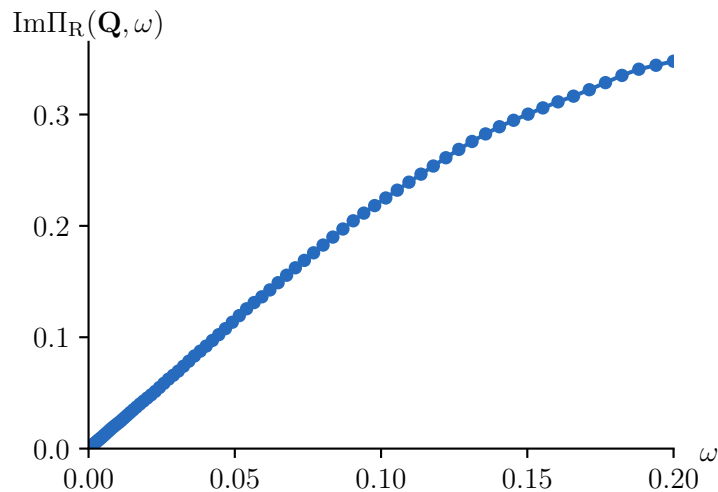


Figure 6.7.: We show the fully converged imaginary part of the polarization $\text{Im} \Pi_{\text{R}}(\mathbf{Q}, \omega)$ as a function of the frequency ω and set the momentum to the numerically determined ordering wave vector $\mathbf{Q} = (2.009, 3.141)$. As expected, we observe a linear regime for small frequencies ω . Parameters: $\beta t_x = 50$, $m/t_x = 0.01$, $\lambda/t_x = 1.0$, $t_y/t_x = 0.3$, $\mu/t_x = -0.55$.

6.4. Renormalized Mass

Remember that we put a lot of effort into analytically calculating the critical exponent p relating the temperature T to the renormalized mass $m(T) \sim T^p$ in the Sections 3 and 5. One main reason for these investigations was that this critical exponent provides an elegant way of comparing the analytical to the numerical results. We therefore computed the boson gap self-consistently for the inverse temperatures $\beta \in \{5, 7.5, 10, 12.5, 15, 20, 25\}$. Unfortunately, this slight computational difference gives rise to a slower convergence which required to increase the number of self-consistency loops from 10 to 20 or even 30. Note that all other parameters were kept fixed, hence $\lambda/t_x = 1.0$, $t_y/t_x = 0.3$ and $\mu/t_x = -0.55$. Note that the renormalized mass can be extracted from the numerical data by

$$m(T) = m_{\text{fix}} + \Pi_{\text{R}}(\mathbf{q}_{\text{max}}, \Omega = 0, T = T_{\text{fix}}) - \Pi_{\text{R}}(\mathbf{q}'_{\text{max}}, \Omega = 0, T \geq T_{\text{fix}}) \quad (6.11)$$

where $m_{\text{fix}} = 0.01$ is the fixed gap at temperature $T_{\text{fix}} = 1/50$ already used in the last sections. Moreover, \mathbf{q}_{max} and \mathbf{q}'_{max} denote the wave vector maximizing the real part of the polarization at temperatures T_{fix} and $T \geq T_{\text{fix}}$, respectively. The numerical values obtained in this way (at full convergence and with the parameters above) are shown in Fig. 6.8. To extract the desired critical exponent, we fit the following theory function [16] to the numerical data points

$$m(T) = a(T^p - T_{\text{fix}}^p) + m_{\text{fix}}. \quad (6.12)$$

with $a, p \in \mathbb{R}$ being the fit parameters. Note that this function is nothing else than the above mention relation $m(T) \sim T^p$ extended by an additive constant (since in the numerics we are not exactly “above” the quantum critical point) and pinned to the point $(T_{\text{fix}}, m_{\text{fix}})$. Fitting yields the parameter $a = 1.544$ and more importantly the critical exponent

$$p = 0.325 \quad (6.13)$$

which is even in quantitative agreement with the analytical determined exponent of $1/3$ from Section 5.4, hence supporting our Eliashberg calculations, the RPA investigations and even our scaling argument.

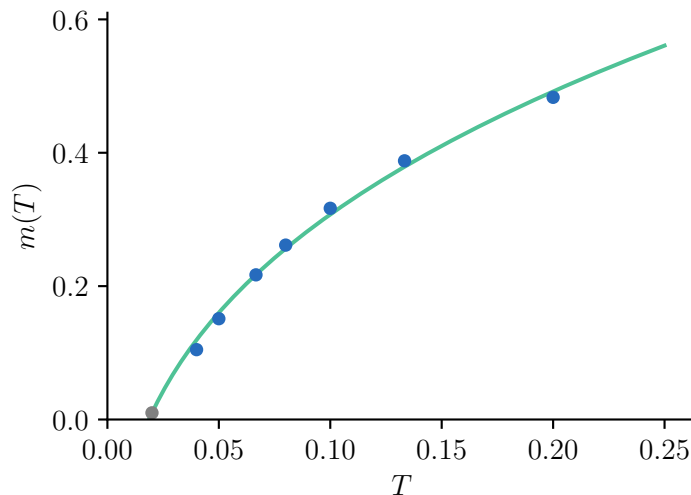


Figure 6.8.: Renormalized mass m in dependence of the temperature T . The blue dots are the results of our numerical investigations at temperatures $T > T_{\text{fix}}$. Note the gray dot at the point $(T_{\text{fix}}, m_{\text{fix}}) = (0.02, 0.01)$ is shown as reminder that the theory curve (6.12) always runs through this point. A fit of the latter to the numerical data reveals the critical exponent $p = 0.325$. Parameters: $\lambda/t_x = 1.0$, $t_y/t_x = 0.3$, $\mu/t_x = -0.55$.

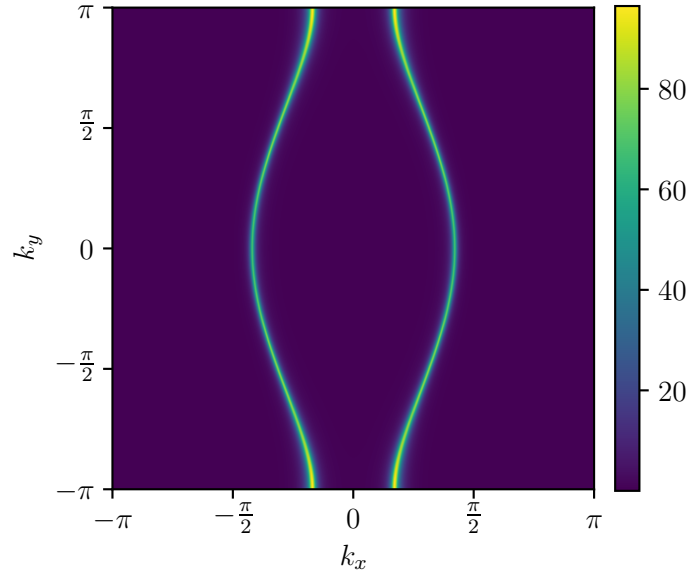
Since we have already determined the numerical solution of the Eliashberg equations at

different temperatures, let us finish our second numerical investigation by a quick look at the spectral function at different temperatures. But first, recapitulate the spectral function [36]

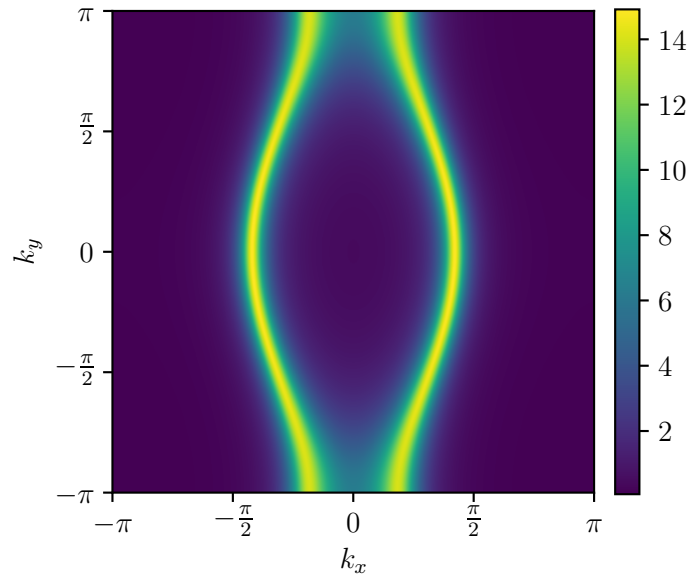
$$A(\mathbf{k}, \omega) := -2 \operatorname{Im} G_{\mathbf{R}}(\mathbf{k}, \omega) \quad (6.14)$$

$$= \frac{-2 \operatorname{Im} \Sigma_{\mathbf{R}}(\mathbf{k}, \omega)}{(\omega - \xi_{\mathbf{k}} - \operatorname{Re} \Sigma_{\mathbf{R}}(\mathbf{k}, \omega))^2 + (\operatorname{Im} \Sigma_{\mathbf{R}}(\mathbf{k}, \omega))^2} \quad (6.15)$$

which is depicted at the Fermi energy $\omega = 0$ for the inverse temperatures $\beta t_x = 5$ and $\beta t_x = 25$ in Fig. 6.9. We observe that the spectral function at the higher inverse temperature $\beta t_x = 25$ still stays relatively sharp, although we notice a slight height variation in k_y -direction. At the lower inverse temperature $\beta t_x = 5$ we find a significantly smeared out spectral function. This is expected and therefore serves as a last consistency check.



(a) $\beta t_x = 25$



(b) $\beta t_x = 5$

Figure 6.9.: Comparison of the spectral function $A(\mathbf{k}, \omega = 0)$ at the Fermi energy for the inverse temperatures $\beta t_x = 25$ (a) and $\beta t_x = 5$ (b). While in (a) the spectral function is still relatively sharp, it strongly smears out at higher temperatures (b). Parameters: $\lambda/t = 0.7$, $t'/t = -0.398$, $\mu/t = -2.175$.

7. Summary & Outlook

In this Master's thesis we studied 2 + 1 dimensional metals in the vicinity of quantum critical points by an Eliashberg approach. These finite temperature calculations for fermions coupled to a real order parameter via a Yukawa-type interaction were performed analytically as well as numerically. Using such a framework we investigated two different models which differed only in the choice of the dispersion relation. Picking either a tight binding or a Fermi sheet-like dispersion relation, we were able to derive expressions for the fermionic as well as the bosonic self-energies evaluated sufficiently close to the hot spots which for example revealed dynamical Fermi surface nesting. Numerically it turns out that the tight binding model has a strong tendency to develop an ordering wave vector $\mathbf{Q} = \mathbf{0}$, making it impossible to study properties of systems displaying charge density wave order. However, the Fermi sheet model clearly displays an ordering wave vector $\mathbf{Q} \neq \mathbf{0}$ and provides unexpected effects like additional regions in momentum space with strongly increased scattering rates. These ridge-like shapes could be identified as $3k_F$ lines and also analytically justified. Furthermore, the analytical and the numerical part were once more compared by computing the critical exponent p , relating the temperature to the mass, for both methods. With $p_{\text{ana}} = 1/3$ and $p_{\text{num}} = 0.325$ we find even quantitatively aligning critical exponents.

Further investigations are conceivable in multiple directions. One could for example try to find a limit in which Eliashberg theory for the model considered in this thesis becomes exact. This obviously is a hard if not impossible task, but it are treatments like the ones recently performed by Berg and Chowdhury that restore some hope [41] and maybe similar techniques can be applied in our case as well. Also numerically it would be interesting to take a closer look at vertex corrections. Similar to [19] an estimate might already be provided by comparing the (projected) leading order vertex correction to the bare coupling constant, hence calculating the ratio

$$\frac{1}{\lambda} \sum_{q,k} \Gamma^{(1)}(q, k) .$$

Deeper insight into the validity and of course also the physics, might be gained by approaching the problem with other numerical methods like e.g. functional renormalization group techniques.

Also from a less formal but more phenomenological point of view there are various interesting follow-up questions left to analyze. One could for example study the tight binding model in more depth with the hope to gain deeper insight into why in all numerical calculations the ordering wave vector shifted to $\mathbf{Q} = \mathbf{0}$ even though the Fermi surface was initially set up with exactly zero curvature at the hot spots, hence seemingly ideal conditions. One could for example increase the chemical potential up to a point where the $2k_F$ lines already exceed the first Brillouin but the Fermi surface does not. Similar to the Fermi-sheet studies, this choice might give rise to finite ordering wave vectors resulting from $2k_F$ line intersections. Additionally, one could ask for the Fermi-sheet model if the encountered $3k_F$ lines can lead to interesting physical effects or even try to observe them experimentally.

A. Additional Derivations

A.1. Retarded Eliashberg Equations

The goal of this section is to show how the Eliashberg equations in the retarded form Eq. (2.12) and (2.13) arise from the imaginary time version Eq. (2.10) and (2.11). Similar derivations can for example be found in [35, 42]. Let us start with the equation for the fermion self-energy by rewriting the Matsubara sum as a contour integral.

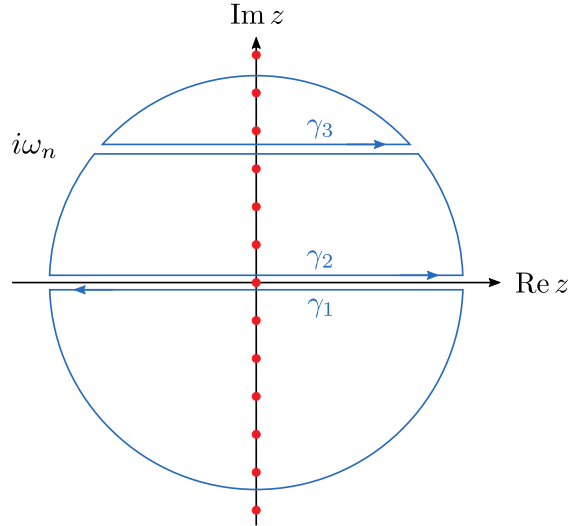


Figure A.1.: The blue lines depict the chosen contour $\gamma := \cup_{i=1}^3 \gamma_i$ to compute the sum over bosonic Matsubara frequencies which are depicted as red dots. Note that the contour avoids the branch cuts at $\text{Im } z = 0$ and $\text{Im } z = i\omega_n$.

The chosen contour γ is shown in Fig. A.1 and leads to

$$\begin{aligned} \Sigma(\mathbf{k}, i\omega_n) &= \frac{\lambda^2}{V} \sum_{\mathbf{q}} \int_{\gamma} \frac{dz}{2\pi i} n_B(z) G(\mathbf{k} - \mathbf{q}, i\omega_n - z) D(\mathbf{q}, z) \\ &\quad + \frac{\lambda^2}{\beta V} \sum_{\mathbf{q}} G(\mathbf{k} - \mathbf{q}, i\omega_n) D(\mathbf{q}, 0). \end{aligned} \quad (\text{A.1})$$

Since the frequency $\Omega_0 = 0$ lies directly on the branch cut at $\text{Im } z = 0$, it needed to be singled out before transforming the sum into an integral. This gives us precisely the

second term. In the limit $R \rightarrow \infty$ only the four vertical paths contribute and we end up with

$$\begin{aligned} \Sigma(\mathbf{k}, i\omega_n) = & \frac{\lambda^2}{V} \sum_{\mathbf{q}} \int_{-\infty}^{\infty} \frac{dz}{2\pi i} \left(n_{\text{B}}(z) G(\mathbf{k} - \mathbf{q}, i\omega_n - z) \{ D_{\text{R}}(\mathbf{q}, z) - D_{\text{A}}(\mathbf{q}, z) \} \right. \\ & \left. + n_{\text{F}}(z) \{ G_{\text{R}}(\mathbf{k} - \mathbf{q}, -z) - G_{\text{A}}(\mathbf{k} - \mathbf{q}, -z) \} D(\mathbf{q}, z + i\omega_n) \right) \quad (\text{A.2}) \end{aligned}$$

where the Ω_0 -term has been canceled by the two vertical paths next to the branch cut at $\text{Im } z = 0$ and advanced as well as retarded propagators have been introduced labeled by the corresponding subscripts. We now perform the analytical continuation $i\omega_n \rightarrow \omega + i0^+$ and exploit that $D_{\text{R}}(\mathbf{q}, z) - D_{\text{A}}(\mathbf{q}, z) = 2i \text{Im } D_{\text{R}}(\mathbf{q}, z)$ as well as $G_{\text{R}}(\mathbf{k} - \mathbf{q}, -z) - G_{\text{A}}(\mathbf{k} - \mathbf{q}, -z) = 2i \text{Im } G_{\text{R}}(\mathbf{k} - \mathbf{q}, -z)$. Taking the imaginary part and shifting $z \rightarrow z + \omega$ in the second integral we finally arrive at

$$\begin{aligned} \text{Im } \Sigma_{\text{R}}(\mathbf{k}, \omega) = & \lambda^2 \int_{\mathbf{q}} \int_{-\infty}^{\infty} \frac{dz}{\pi} (n_{\text{B}}(z) + n_{\text{F}}(z - \omega)) \\ & \cdot \text{Im } G_{\text{R}}(\mathbf{k} - \mathbf{q}, \omega - z) \text{Im } D_{\text{R}}(\mathbf{q}, z) \quad (\text{A.3}) \end{aligned}$$

where $\int_{\mathbf{q}} := \int \frac{d^2q}{4\pi^2}$. This is precisely the Eliashberg equation (2.12) for the fermion self-energy in the retarded version what we have been looking for.

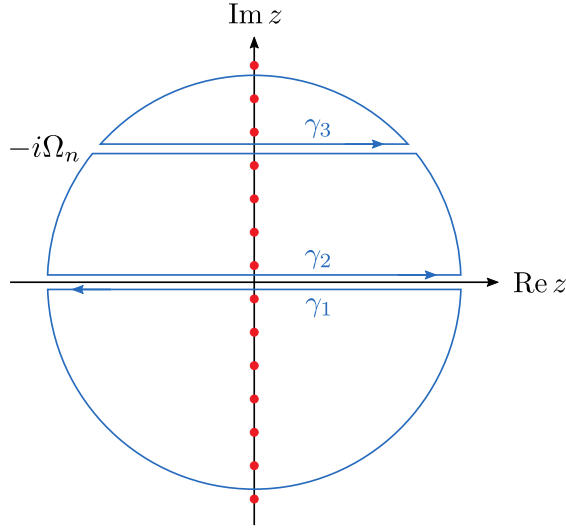


Figure A.2.: The blue lines depict the chosen contour $\gamma := \cup_{i=1}^3 \gamma_i$ to compute the sum over fermionic Matsubara frequencies which are depicted as red dots. Note that the contour avoids the branch cuts at $\text{Im } z = 0$ and $\text{Im } z = -i\Omega_n$.

The equation for the retarded polarization is even easier to derive, since none of the frequencies lie on any of the branch cuts which is depicted in Fig. A.2. We therefore

can directly turn the Matsubara sum into the contour integral

$$\Pi(\mathbf{k}, i\Omega_n) = \frac{2\lambda^2}{V} \sum_{\mathbf{q}} \int_{\gamma} \frac{dz}{2\pi i} n_F(z) G(\mathbf{k} + \mathbf{q}, i\Omega_n + z) G(\mathbf{q}, z). \quad (\text{A.4})$$

Note that the -1 from the fermionic loop cancels with an additional factor of -1 resulting from the residues of n_F . Now again take the limit $R \rightarrow \infty$, perform the analytical continuation $i\Omega_n \rightarrow \Omega + i0^+$ and take the imaginary part resulting in the expression

$$\begin{aligned} \text{Im } \Pi_{\text{R}}(\mathbf{k}, \Omega) &= 2\lambda^2 \int_{\mathbf{q}} \int_{-\infty}^{\infty} \frac{dz}{\pi} (n_F(z) - n_F(z + \Omega)) \\ &\quad \cdot \text{Im } G_{\text{R}}(\mathbf{k} + \mathbf{q}, \Omega + z) \text{Im } G_{\text{R}}(\mathbf{q}, z) \end{aligned} \quad (\text{A.5})$$

which is exactly the Eliashberg equation (2.13) for the polarization in the retarded version.

A.2. Mass Term in RPA

Consider the (divergent) integral

$$I(\beta) := \int d^2k \frac{1}{k_x} \cdot \frac{1}{\exp(\beta(k_x + k_y^2)) + 1} \quad (\text{A.6})$$

$$= \int_{-\infty}^{\infty} \frac{dk_x}{k_x} \int_0^{\infty} dk_y \frac{2}{\exp(\beta(k_x + k_y^2)) + 1} \quad (\text{A.7})$$

$$= \int_{-\infty}^{\infty} \frac{dk_x}{\sqrt{\beta}k_x} \int_0^{\infty} d\xi \frac{\xi^{-1/2}}{\exp(\beta k_x + \xi) + 1} \quad (\text{A.8})$$

where we used the substitution $\xi := \beta k_y^2$ in the last step. We just encountered the so called Fermi-Dirac integral $F_{-1/2}$ and can therefore continue

$$I(\beta) = \int_{-\infty}^{\infty} \frac{dk_x}{\sqrt{\beta}k_x} F_{-1/2}(-\beta k_x) \cdot \Gamma(-\frac{1}{2} + 1) \quad (\text{A.9})$$

$$= \int_{-\infty}^{\infty} dk_x \frac{-\sqrt{\pi} \cdot \text{Li}_{1/2}(-\exp(-\beta k_x))}{\sqrt{\beta}k_x} \quad (\text{A.10})$$

where $\text{Li}_{1/2}$ is the polylogarithm of order $1/2$. Let us keep this expression in mind and turn our attention for a minute to the $\beta \rightarrow \infty$ limit. Using the theta function θ , eq. A.6 can be written as

$$I(\beta \rightarrow \infty) = \int d^2k \frac{1}{k_x} \cdot \theta(-k_x - k_y^2) \quad (\text{A.11})$$

$$= \int_{-\infty}^0 dk_x \int_{-\infty}^{\infty} dk_y \frac{\theta(-k_x - k_y^2)}{k_x} \quad (\text{A.12})$$

Since the k_y -integral is nothing else than the width of the parabola (defined through $k_x = -k_y^2$) at height k_x , we conclude

$$I(\beta \rightarrow \infty) = \int_{-\infty}^0 dk_x \frac{2\sqrt{-k_x}}{k_x} \quad (\text{A.13})$$

$$= - \int_0^{\infty} dk_x \frac{2}{\sqrt{k_x}}. \quad (\text{A.14})$$

To obtain a finite result we consider the renormalized polarization and therefore compute

$$I(\beta) - I(\beta \rightarrow \infty) = \int_{-\infty}^{\infty} dk_x \frac{-\sqrt{\pi} \cdot \text{Li}_{1/2}(-\exp(-\beta k_x))}{\sqrt{\beta} k_x} + \int_0^{\infty} dk_x \frac{2}{\sqrt{k_x}} \quad (\text{A.15})$$

$$= \frac{1}{\sqrt{\beta}} \int_0^{\infty} dx \frac{-\sqrt{\pi} \cdot \text{Li}_{1/2}(-e^{-x}) + \sqrt{\pi} \cdot \text{Li}_{1/2}(-e^x) + 2\sqrt{x}}{x} \quad (\text{A.16})$$

$$= \frac{c}{\sqrt{\beta}} \quad (\text{A.17})$$

with the numerical constant $c \approx 3.37$. We conclude that the mass therefore reads

$$m^{(\text{RPA})}(\beta) = \frac{\lambda^2}{\sqrt{2\kappa}\pi^2 v_F} (I(\beta) - I(\beta \rightarrow \infty)) \quad (\text{A.18})$$

$$= \frac{\lambda^2}{\sqrt{2\kappa}\pi^2 v_F} \cdot \frac{c}{\sqrt{\beta}}. \quad (\text{A.19})$$

A.3. Mass Term in Eliashberg Theory

Let us start from the (divergent) expression

$$\text{Re } \Pi_{+,R}(\mathbf{0}, 0) = 4\lambda^2 \int_{\mathbf{q}} \int_{-\infty}^0 \frac{dz}{\pi} \frac{z - \xi_{+,q}}{(z - \xi_{+,q})^2 + \gamma_+^2} \cdot \frac{-\gamma_+}{(z - \xi_{+,-q})^2 + \gamma_+^2}. \quad (\text{A.20})$$

Performing the substitutions $\omega := z - \xi_{+,q}$, $k_x := v_F q_x$ and $k_y := \sqrt{\kappa/2} q_y$ result in

$$\text{Re } \Pi_{+,R}(\mathbf{0}, 0) = -\frac{\sqrt{2}\lambda^2}{v_F \pi^3 \sqrt{\kappa}} \int d^2 k \int_{-\infty}^{-k_x - k_y^2} d\omega \frac{\omega}{\omega^2 + \gamma_+^2} \cdot \frac{\gamma_+}{(\omega + 2k_x)^2 + \gamma_+^2}. \quad (\text{A.21})$$

Solving the frequency integral gives

$$\begin{aligned} \text{Re } \Pi_{+,R}(\mathbf{0}, 0) = & -\frac{\sqrt{2}\lambda^2}{v_F \pi^3 \sqrt{\kappa}} \int d^2 k \frac{1}{8k_x(\gamma_+^2 + k_x^2)} \left[2\gamma_+^2 \arctan\left(\frac{\omega}{\gamma_+}\right) \right. \\ & - (2\gamma_+^2 + 4k_x^2) \arctan\left(\frac{\omega + 2k_x}{\gamma_+}\right) \\ & \left. + \gamma_+ k_x \left(\ln(\gamma_+^2 + \omega^2) - \ln(\gamma_+^2 + (\omega + 2k_x)^2) \right) \right] \Bigg|_{-\infty}^{-k_x - k_y^2}. \quad (\text{A.22}) \end{aligned}$$

Careful evaluation leads to the much simpler expression

$$\text{Re } \Pi_{+,R}(\mathbf{0}, 0) = \frac{\lambda^2}{v_F \pi^3 \sqrt{2\kappa}} \int d^2k \frac{\arctan\left(\frac{k_x + k_y^2}{\gamma_+}\right)}{k_x} \quad (\text{A.23})$$

which is of course still divergent. Hence, we take the zero temperature limit

$$\text{Re } \Pi_{+,R}(\mathbf{0}, 0, T = 0) = \frac{\lambda^2}{v_F \pi^3 \sqrt{2\kappa}} \int d^2k \frac{\frac{\pi}{2} \text{sgn}(k_x + k_y^2)}{k_x}. \quad (\text{A.24})$$

The renormalized mass is now given by

$$m(T) = \text{Re } \Pi_{+,R}(\mathbf{0}, 0, T = 0) - \text{Re } \Pi_{+,R}(\mathbf{0}, 0) \quad (\text{A.25})$$

$$= \frac{\lambda^2}{v_F \pi^3 \sqrt{2\kappa}} \sqrt{\gamma_+} \int d^2q \frac{\text{sgn}(q_x + q_y^2) - \arctan(q_x + q_y^2)}{q_x} \quad (\text{A.26})$$

where we substituted both integrals by $q_x := k_x/\gamma_+$ and $q_y := k_y/\sqrt{\gamma_+}$. The remaining integral evaluates to

$$\int d^2q \frac{\text{sgn}(q_x + q_y^2) - \arctan(q_x + q_y^2)}{q_x} \quad (\text{A.27})$$

$$= i\pi \int_{-\infty}^{\infty} dq_x \frac{\sqrt{q_x - i}}{q_x} - i\pi \int_{-\infty}^{\infty} dq_x \frac{\sqrt{q_x + i}}{q_x} + 2\pi \int_0^{\infty} dq_x \frac{1}{\sqrt{q_x}} \quad (\text{A.28})$$

$$= \sqrt{2} \cdot 2\pi^2. \quad (\text{A.29})$$

Hence, we find the promised result

$$m(T) = \frac{2\lambda^2}{\sqrt{\kappa}\pi v_F} \sqrt{\gamma_+}. \quad (\text{A.30})$$

A.4. Derivatives in the Sommerfeld Expansion

Consider the following derivative (and recall the definition of f from Section 3.3):

$$\frac{d^{2n-1} f_{(\gamma_+ k_x, \sqrt{\gamma_+} k_y)}(z)}{dz^{2n-1}} = \gamma_+^{-2} \cdot \frac{d^{2n-1}}{dz^{2n-1}} \left(\frac{z/\gamma_+ - \xi_{+, \mathbf{k}}}{(z/\gamma_+ - \xi_{+, \mathbf{k}})^2 + 1} \cdot \frac{-1}{(z/\gamma_+ - \xi_{+, -\mathbf{k}})^2 + 1} \right) \quad (\text{A.31})$$

Using the function $g_{\mathbf{k}}$ (defined through the bracketed expression above) we are able to write

$$\frac{d^{2n-1} f_{(\gamma_+, k_x, \sqrt{\gamma_+} k_y)}(z)}{dz^{2n-1}} = \gamma_+^{-2} \cdot \frac{d^{2n-1}}{dz^{2n-1}} g_{\mathbf{k}} \left(\frac{z}{\gamma_+} \right) \quad (\text{A.32})$$

$$= \gamma_+^{-2} \cdot \frac{\partial^{2n-1}}{\partial \left(\frac{z}{\gamma_+} \right)^{2n-1}} g_{\mathbf{k}} \left(\frac{z}{\gamma_+} \right) \cdot \gamma_+^{-2n+1} \quad (\text{A.33})$$

Evaluating at $z = 0$ finally leads to

$$\left. \frac{d^{2n-1} f_{(\gamma_+, k_x, \sqrt{\gamma_+} k_y)}(z)}{dz^{2n-1}} \right|_{z=0} = \gamma_+^{-2n-1} \cdot \left. \frac{\partial^{2n-1}}{\partial z^{2n-1}} g_{\mathbf{k}}(z) \right|_{z=0} \quad (\text{A.34})$$

$$=: \gamma_+^{-2n-1} \cdot h(\mathbf{k}) \quad (\text{A.35})$$

involving a momentum-dependent function h .

A.5. Imaginary Part of Polarization

Let us recall the integral to be solved for $a \neq 0$

$$J(\mathbf{k}) := \int_{-\infty}^{\infty} dq_y \frac{1}{\left(\frac{|a|}{2\gamma_+ v_{F,-}} \cdot q_y^2 - \frac{\text{sgn}(a)\kappa_+ k_y}{\gamma_+} \cdot q_y + \frac{\text{sgn}(a)\xi_{+,\mathbf{k}}}{\gamma_+} \right)^2 + 1} \quad (\text{A.36})$$

and perform the substitution $x := \sqrt{\frac{|a|}{2\gamma_+ v_{F,-}}} \cdot q_y$ which gives

$$J(\mathbf{k}) = \sqrt{\frac{2\gamma_+ v_{F,-}}{|a|}} \int_{-\infty}^{\infty} dx \frac{1}{(x^2 + bx + c)^2 + 1} \quad (\text{A.37})$$

with $b := -\text{sgn}(a)\kappa_+ k_y \cdot \sqrt{\frac{2v_{F,-}}{\gamma_+ |a|}}$ and $c := \frac{\text{sgn}(a)\xi_{+,\mathbf{k}}}{\gamma_+}$. With the substitution $x \rightarrow x - \frac{b}{2}$ our expression reduces to

$$J(\mathbf{k}) = \sqrt{\frac{2\gamma_+ v_{F,-}}{|a|}} \int_{-\infty}^{\infty} dx \frac{1}{(x^2 + d)^2 + 1} \quad (\text{A.38})$$

where $d := c - \frac{b^2}{4}$. This can now be easily solved by the residue theorem eventually resulting in

$$J(\mathbf{k}) = \sqrt{\frac{2\gamma_+ v_{F,-}}{|a|}} \cdot \frac{\pi}{\sqrt{2}} \cdot \frac{\sqrt{\sqrt{d^2 + 1} - d}}{\sqrt{d^2 + 1}}. \quad (\text{A.39})$$

Now we plug $d = \frac{\text{sgn}(a)}{\gamma_+} \left(\xi_{+, \mathbf{k}} - \frac{\kappa_+^2 v_{\text{F}, -}}{2a} k_y^2 \right) =: \frac{\eta_{\mathbf{k}}}{\gamma_+}$ back into our expression yielding

$$J(\mathbf{k}) = \pi \gamma_+ \cdot \sqrt{\frac{v_{\text{F}, -}}{|a|}} \cdot \frac{\sqrt{\sqrt{\eta_{\mathbf{k}}^2 + \gamma_+^2} - \eta_{\mathbf{k}}}}{\sqrt{\eta_{\mathbf{k}}^2 + \gamma_+^2}} \quad (\text{A.40})$$

which is exactly the expression we have been using in advance in Section 5.3.

References

- ¹M. Vojta, “Quantum phase transitions”, Reports on Progress in Physics **66**, 2069–2110 (2003).
- ²S. Sachdev, *Quantum phase transitions*, 2nd ed. (Cambridge University Press, 2011).
- ³L. P. Kadanoff, *Statistical physics: statics, dynamics and renormalization* (World Scientific Publishing Company, 2000).
- ⁴M. Heyl, “Dynamical quantum phase transitions: a review”, Reports on Progress in Physics **81**, 054001 (2018).
- ⁵H. Meyer-Ortmanns, “Phase transitions in quantum chromodynamics”, Rev. Mod. Phys. **68**, 473–598 (1996).
- ⁶K. Fukushima and T. Hatsuda, “The phase diagram of dense QCD”, Reports on Progress in Physics **74**, 014001 (2010).
- ⁷S. A. Hartnoll, J. Polchinski, E. Silverstein and D. Tong, “Towards strange metallic holography”, JHEP **04**, 120 (2010).
- ⁸P. Fulde, *Correlated electrons in quantum matter* (World Scientific, 2012).
- ⁹J. A. Hertz, “Quantum critical phenomena”, Phys. Rev. B **14**, 1165–1184 (1976).
- ¹⁰A. J. Millis, “Effect of a nonzero temperature on quantum critical points in itinerant fermion systems”, Phys. Rev. B **48**, 7183–7196 (1993).
- ¹¹S.-S. Lee, “Low-energy effective theory of Fermi surface coupled with $U(1)$ gauge field in $2 + 1$ dimensions”, Phys. Rev. B **80**, 165102 (2009).
- ¹²M. A. Metlitski and S. Sachdev, “Quantum phase transitions of metals in two spatial dimensions. I. Ising-nematic order”, Phys. Rev. B **82**, 075127 (2010).
- ¹³J. Sýkora, T. Holder and W. Metzner, “Fluctuation effects at the onset of the $2k_F$ density wave order with one pair of hot spots in two-dimensional metals”, Phys. Rev. B **97**, 155159 (2018).
- ¹⁴T. Holder and W. Metzner, “Non-fermi-liquid behavior at the onset of incommensurate $2k_f$ charge- or spin-density wave order in two dimensions”, Phys. Rev. B **90**, 161106 (2014).
- ¹⁵B. L. Altshuler, L. B. Ioffe and A. J. Millis, “Critical behavior of the $T = 0$ $2k_F$ density-wave phase transition in a two-dimensional Fermi liquid”, Phys. Rev. B **52**, 5563–5572 (1995).

- ¹⁶J. Halbinger, D. Pimenov and M. Punk, “Incommensurate $2k_F$ density wave quantum criticality in two-dimensional metals”, *Phys. Rev. B* **99**, 195102 (2019).
- ¹⁷A. Migdal, “Interaction between electrons and lattice vibrations in a normal metal”, *Sov. Phys. JETP* **7**, 996–1001 (1958).
- ¹⁸G. Eliashberg, “Interactions between electrons and lattice vibrations in a superconductor”, *Sov. Phys. JETP* **11**, 696–702 (1960).
- ¹⁹M. Punk, “Nematic fluctuations and their wave vector in two-dimensional metals”, *Phys. Rev. B* **91**, 115131 (2015).
- ²⁰M. Punk, “Finite-temperature scaling close to Ising-nematic quantum critical points in two-dimensional metals”, *Phys. Rev. B* **94**, 195113 (2016).
- ²¹J. Polchinski, “Low-energy dynamics of the spinon-gauge system”, *Nuclear Physics B* **422**, 617–633 (1994).
- ²²G.-H. Gweon, J. Denlinger, J. Clack, J. Allen, C. Olson, E. DiMasi, M. Aronson, B. Foran and S. Lee, “Direct observation of complete fermi surface, imperfect nesting, and gap anisotropy in the high-temperature incommensurate charge-density-wave compound SmTe_3 ”, *Physical review letters* **81**, 886 (1998).
- ²³A. Fang, N. Ru, I. Fisher and A. Kapitulnik, “Stm studies of TbTe_3 : evidence for a fully incommensurate charge density wave”, *Physical review letters* **99**, 046401 (2007).
- ²⁴J. A. Wilson, F. Di Salvo and S. Mahajan, “Charge-density waves and superlattices in the metallic layered transition metal dichalcogenides”, *Advances in Physics* **24**, 117–201 (1975).
- ²⁵G. Scholz, O. Singh, R. Frindt and A. Curzon, “Charge density wave commensurability in $2\text{H} - \text{TaS}_2$ and Ag_xTaS_2 ”, *Solid State Communications* **44**, 1455–1459 (1982).
- ²⁶P. Chen, W. W. Pai, Y.-H. Chan, V. Madhavan, M.-Y. Chou, S.-K. Mo, A.-V. Fedorov and T.-C. Chiang, “Unique gap structure and symmetry of the charge density wave in single-layer VSe_2 ”, *Physical review letters* **121**, 196402 (2018).
- ²⁷D. Pimenov, “Beyond the Landau-Ginzburg-Wilson paradigm”, PhD thesis (Ludwig Maximilians University of Munich, 2019).
- ²⁸J. Halbinger, “Quantum phase transition to incommensurate $2k_F$ charge density wave order”, MA thesis (Ludwig Maximilians University of Munich, 2019).
- ²⁹R. Peierls and R. Peierls, *Surprises in theoretical physics*, Princeton Series in Physics (Princeton University Press, 1979).
- ³⁰Y. Wang and A. Chubukov, “Quantum-critical pairing in electron-doped cuprates”, *Phys. Rev. B* **88**, 024516 (2013).
- ³¹D. Bergeron, D. Chowdhury, M. Punk, S. Sachdev and A.-M. S. Tremblay, “Breakdown of Fermi liquid behavior at $(\pi, \pi) = 2k_F$ the spin-density wave quantum-critical point: The case of electron-doped cuprates”, *Phys. Rev. B* **86**, 155123 (2012).

- ³²A. Abanov, A. V. Chubukov and J. Schmalian, “Quantum-critical theory of the spin-fermion model and its application to cuprates: normal state analysis”, *Advances in Physics* **52**, 119–218 (2003).
- ³³D. Dalidovich and S.-S. Lee, “Perturbative non-Fermi liquids from dimensional regularization”, *Physical Review B* **88**, 245106 (2013).
- ³⁴J. Rech, C. Pépin and A. V. Chubukov, “Quantum critical behavior in itinerant electron systems: Eliashberg theory and instability of a ferromagnetic quantum critical point”, *Phys. Rev. B* **74**, 195126 (2006).
- ³⁵A. Altland and B. D. Simons, *Condensed matter field theory*, 2nd ed. (Cambridge University Press, 2010).
- ³⁶G. D. Mahan, *Many-particle physics*, 2nd (Plenum Press, 1993).
- ³⁷B. L. Altshuler, L. B. Ioffe and A. J. Millis, “Low-energy properties of fermions with singular interactions”, *Phys. Rev. B* **50**, 14048–14064 (1994).
- ³⁸S. A. Hartnoll, R. Mahajan, M. Punk and S. Sachdev, “Transport near the Ising-nematic quantum critical point of metals in two dimensions”, *Phys. Rev. B* **89**, 155130 (2014).
- ³⁹N. Ashcroft and N. Mermin, *Solid state physics* (Brooks/Cole Publishing, 2003).
- ⁴⁰T. Holder and W. Metzner, “Incommensurate nematic fluctuations in two-dimensional metals”, *Phys. Rev. B* **85**, 165130 (2012).
- ⁴¹D. Chowdhury and E. Berg, “The unreasonable effectiveness of Eliashberg theory for pairing of non-Fermi liquids”, arXiv e-prints (2019).
- ⁴²A. A. Abrikosov, L. P. Gorkov and I. E. Dzyaloshinski, *Methods of quantum field theory in statistical physics* (Dover Publications, 1975).

Erklärung:

Hiermit erkläre ich, die vorliegende Arbeit selbständig verfasst zu haben und keine anderen als die in der Arbeit angegebenen Quellen und Hilfsmittel benutzt zu haben.

München, den 10. März 2020

David Jonas Moser